minerals

MDPI

Article

The System KCl–$CaCO_3$–$MgCO_3$ at 3 GPa

Anton Shatskiy [1,*], Ivan V. Podborodnikov [1], Anton V. Arefiev [1] and Konstantin D. Litasov [2]

[1] Vernadsky Institute of Geochemistry and Analytical Chemistry, Russian Academy of Science, Moscow 119991, Russia
[2] Vereshchagin Institute for High Pressure Physics, Russian Academy of Science, Troitsk, Moskow 108840, Russia
* Correspondence: shatskiyantonf@gmail.com or shatskiy@geokhi.ru; Tel.: +7-(913)-385-61-29

Abstract: Inclusions in mantle minerals and xenoliths from kimberlites worldwide derived from depths exceeding 100 km vary in composition from alkali-rich saline to carbonatitic. Despite the wide distribution of these melts and their geochemical importance as metasomatic agents that altered the mineralogy and geochemistry of mantle rocks, the *P*-*T* range of stability of these melts remains largely undefined. Here we report new experimental data on phase relations in the system KCl–$CaCO_3$–$MgCO_3$ at 3 GPa obtained using a multianvil press. We found that the KCl–$CaCO_3$ and KCl–$MgCO_3$ binaries have the eutectic type of *T*-*X* diagrams. The KCl-calcite eutectic is situated at K2# 56 and 1000 °C, while the KCl-magnesite eutectic is located at K2# 79 and 1100 °C, where K2# = 2KCl/(2KCl + $CaCO_3$ + $MgCO_3$) × 100 mol%. Just below solidus, the KCl–$CaCO_3$–$MgCO_3$ system is divided into two partial ternaries: KCl + magnesite + dolomite and KCl + calcite–dolomite solid solutions. Both ternaries start to melt near 1000 °C. The minimum on the liquidus/solidus surface corresponds to the KCl + $Ca_{0.73}Mg_{0.27}CO_3$ dolomite eutectic situated at K2#/Ca# 39/73, where Ca# = 100·Ca/(Ca + Mg) × 100 mol%. At bulk Ca# ≤ 68, the melting is controlled by a ternary peritectic: KCl + dolomite = magnesite + liquid with K2#/Ca# 40/68. Based on our present and previous data, the KCl + dolomite melting reaction, expected to control solidus of KCl-bearing carbonated eclogite, passes through 1000 °C at 3 GPa and 1200 °C at 6 GPa and crossovers a 43-mW/m^2 geotherm at a depth of 120 km and 37-mW/m^2 geotherm at a depth of 190 km.

Keywords: chloride; carbonate; KCl; melting; *T*-*X* diagram; Earth's mantle

check for updates

Citation: Shatskiy, A.; Podborodnikov, I.V.; Arefiev, A.V.; Litasov, K.D. The System KCl–$CaCO_3$–$MgCO_3$ at 3 GPa. *Minerals* **2023**, *13*, 248. https://doi.org/10.3390/min13020248

Academic Editor: Lidong Dai

Received: 9 January 2023
Revised: 22 January 2023
Accepted: 7 February 2023
Published: 9 February 2023

1. Introduction

Alkaline chlorides, along with carbonates and water, are an important constituent of melts or high-density fluids found as inclusions in mantle xenoliths and minerals from kimberlites, as well as diamonds from kimberlites and placers around the world [1–19]. These melts are considered as a crystallization medium for natural diamonds [1,9,20]; metasomatic agents that changed the geochemistry of mantle rocks [9,21], and parental melts for kimberlites [21–23]. *P*-*T* estimates of the formation of xenoliths from kimberlites and lamproites with inclusions of alkaline chloride–carbonate melts indicate that the range of their existence in the subcontinental lithospheric mantle (SCLM) covers depths of 110–230 km [11,24,25]. In this regard, it is of interest to study the phase relationships in alkaline carbonate–chloride systems at pressures of 3–6 GPa corresponding to these depths. Previously, a number of experimental works were devoted to the study of phase relationships, in particular liquid immiscibility, in complex potassium chloride–carbonate–silicate ± H_2O systems [26–31]. However, most of these experiments were concentrated on pressures corresponding to the base of SCLM or deeper conditions. In addition, we have recently completed a systematic study of the *T*-*X* phase diagrams of the KCl–$CaCO_3$–$MgCO_3$ and NaCl–$CaCO_3$–$MgCO_3$ systems at 6 GPa [32–35].

With this work, we expand the range of studies of these systems to the shallow mantle and present new experimental results on phase relations in the KCl–$CaCO_3$–$MgCO_3$ system at 3 GPa.

2. Materials and Methods

Experiments were run on a multianvil DIA-type press "Discoverer-1500". 26-mm tungsten carbide cubes "Fujilloy TN-05" (Fuji Die Co., Ltd., Tokyo, Japan) with 12 mm truncations were used as inner stage anvils. The high-pressure cell was shaped as octahedra with an edge length of 20.5 mm. Parts of the cell were ground from semisintered ZrO_2 ceramics (OZ-8C, MinoYogyo Co., Ltd., Nagoya, Japan) [36]. Pyrophyllite gaskets 4 mm both in thickness and width were fixed on anvil flanks near truncations using rice glue [37]. Heating was achieved using a tubular graphite heater 4.0/4.5 mm in diameter and 11 mm in length. The temperature was controlled using a $W_{97\%}Re_{3\%}$-$W_{75\%}Re_{25\%}$ thermocouple in a temperature mode.

The cell contained four graphite cassettes. Each cassette had four cylindrical cavities (holes) 0.9 mm in diameter and 1.1 mm in depth. The holes were filled with powdered starting mixtures listed in Tables 1 and 2. The loaded holes were corked up by graphite caps 0.2 mm in thickness.

The starting mixtures were prepared by blending reagent-grade KCl, $CaCO_3$ (<0.01 wt% impurities), and natural magnesite from Brumado, Bahia (Brazil) (<0.1 wt% impurities) in agate mortar under acetone. Special care has been taken to minimize sample contamination with water. Cassettes with starting mixtures were dried at 300 °C for 1 h. Ceramic parts were fired at 1000 °C for 1 h. The prepared sample assemblages were stored in vacuum at 200 °C for $\leq$12 h before the experiment. The indoor humidity during the preparation of experiments did not exceed 15%–35%.

The experiment was carried out by increasing the press load to 3 MN (corresponding to a pressure of 3 GPa) for 2.5 h; heating to a target temperature at a rate of 50 °C/min; annealing at a fixed temperature and pressure; turning off the heater power, accompanied by a temperature drop below 200 °C within a few seconds; decompression for 3 h.

After the experiment, graphite cassettes were cut using a low-speed diamond saw in an axial direction. Then obtained specimens were fixed on a double-side tape and filled with epoxy in a plexiglass holder. The samples were ground using sandpapers 400 (37)-, 1000 (13)-, and 1500 (9)-mesh (μm) under WD-40 lubricant and finally polished using a 3-μm diamond paste on a satin close. The polished specimens were cleaned and stored in benzine before carbon coating.

The samples were studied using an electron microscope Tescan MIRA 3 LMU (Tescan Orsay Holding, Brno-Kohoutovice, Czech Republic), coupled with an energy dispersive X-ray spectrometer (EDS) INCA Energy 450 (Oxford Instruments Nanoanalysis Ltd., High Wycombe, UK) [38]. Energy-dispersive X-ray spectra were collected in an electron beam-rastering mode, in which the stage was stationary while the electron beam moved over the surface area, with dimensions 5–100 μm (for quenched melt) at 20 kV accelerating voltage and 1.5 nA beam current. The live counting time for X-ray spectra was 20 s.

$CaCO_3$ polymorphs were identified using a Horiba Jobin Yvon LabRAM HR800 Raman microspectrometer (HORIBA Jobin Yvon SAS, Longjumeau, France) equipped with a multi-channel LN/CCD detector with a resolution of 1024 pixels and 532.1 nm solid-state laser.

Table 1. Phase compositions (mol%) in run D321 at 900 °C and 72 h.

#	Phases	K2#	Ca#	Cl2#	*n*	MgO	CaO	K_2O	Cl_2	CO_2
1-1	Bulk	**20**	**100**	20	-	-	40.0	10.0	10.0	40.0
	KCl	100(0)	-	100(0)	6	b.d.l.	b.d.l.	50.2(2)	49.8(3)	-
	Arg	-	100(0)	-	6	b.d.l.	50.0(2)	b.d.l.	b.d.l.	50.0(2)
1-2	Bulk	**80**	**100**	80	-	-	10.0	40.0	40.0	10.0
	KCl	100(0)	-	100(0)	5	b.d.l.	b.d.l.	50.2(2)	49.8(3)	-
	Arg	-	100(0)	-	5	b.d.l.	48.8(8)	1.26(80)	1.19(80)	48.8(8)
1-3	Bulk	**5**	**95**	5	-	2.38	45.1	2.50	2.50	47.5
	KCl	99(0)	-	100(0)	5	b.d.l.	0.64(21)	50.0(1)	49.1(2)	-
	Cal	-	97(2)	-	9	1.64(93)	48.3(9)	b.d.l.	b.d.l.	50.0(0)
4-3	Bulk	**40**	**92**	40	-	2.40	27.6	20.0	20.0	30.0
	KCl	100	-	100	4	b.d.l.	b.d.l.	50.3(2)	49.6(1)	b.d.l.
	Cal	-	94	-	4	3.09	46.6	0.32	0.23	49.8
3-4	Bulk	**60**	**80**	60	-	4.00	16.0	30.0	30.0	20.0
	KCl	100	-	100	4	b.d.l.	b.d.l.	50.3(2)	49.7(1)	-
	Dol	-	81(2)	-	7	9.50(1.22)	40.0(1.3)	0.46(14)	0.40(15)	49.6(2)
1-4	Bulk	**8**	**75**	8	-	11.5	34.5	4.0	4.0	46.0
	KCl	99(0)	-	100(0)	5	b.d.l.	0.42(12)	50.1(1)	49.3(1)	-
	Dol	-	75(14)	-	12	12.4(7.1)	37.6(7.0)	b.d.l.	b.d.l.	50.0(0)
4-1	Bulk	**50**	**75**	50	-	6.3	18.8	25.0	25.0	25.0
	KCl	100(0)	-	100(0)	5	b.d.l.	b.d.l.	50.3(1)	49.7(1)	-
	Dol	-	75(6)	-	5	12.5(3.2)	37.1(3.4)	0.44(19)	0.38(26)	49.6(3)
4-2	Bulk	**10**	**60**	10	-	18.0	27.0	5.0	5.0	45.0
	KCl	100	-	100	1	b.d.l.	b.d.l.	50.2	49.8	-
	Ca-Dol	-	71(14)	-	10	14.6(6.9)	35.3(6.9)	b.d.l.	b.d.l.	49.9(1)
	Dol	-	54(1)	-	9	23.0(4)	27.0(4)	b.d.l.	b.d.l.	50.0(1)
2-1	Bulk	**43**	**54**	43	-	13.1	15.4	21.5	21.5	28.5
	KCl	100(0)	-	100(0)	9	b.d.l.	b.d.l.	50.2(1)	49.4(2)	-
	Dol	-	53	-	1	23.5	26.5	b.d.l.	b.d.l.	50.0
2-2	Bulk	**8**	**42**	8	-	26.7	19.3	4.00	4.00	46.0
	KCl	100(0)	-	100(0)	5	b.d.l.	b.d.l.	50.3(1)	49.7(1)	-
	Mgs	-	1(0)	-	5	49.7(0)	0.27(3)	b.d.l.	b.d.l.	50.0(0)
2-3	Bulk	**40**	**33**	40	-	20.1	9.90	20.0	20.0	30.0
	KCl	100(1)	-	100(0)	7	b.d.l.	b.d.l.	50.2(2)	49.8(5)	-
	Dol	-	-	-	+	-	-	-	-	-
	Mgs	-	1(1)	-	5	49.5(4)	0.41(34)	b.d.l.	b.d.l.	50.0(0)
2-4	Bulk	**20**	**37**	20	-	25.2	14.8	10.0	10.0	40.0
	KCl	100(0)	-	100(0)	8	b.d.l.	b.d.l.	50.1(2)	49.9(4)	-
	Dol	-	-	-	+	-	-	-	-	-
	Mgs	-	1(0)	-	6	49.7(0)	0.27(3)	b.d.l.	b.d.l.	50.0(0)
4-4	Bulk	**10**	**25**	10	-	33.8	11.2	5.00	5.00	45.0
	KCl	100(1)	-	100(1)	5	b.d.l.	b.d.l.	50.3(3)	49.7(3)	-
	Dol	-	49	-	2	25.5	24.5	b.d.l.	b.d.l.	50.0
	Mgs	-	1(0)	-	5	49.6(3)	0.44(29)	b.d.l.	b.d.l.	50.0(0)
2-1	Bulk	**30**	**50**	30	-	17.5	17.5	15.0	15.0	35.0
	KCl	100(0)	-	100(0)	5	b.d.l.	b.d.l.	50.1(0)	49.9(0)	-
	Dol	-	52(1)	-	5	24.1(6)	25.9(6)	b.d.l.	b.d.l.	50.0(0)
3-1	Bulk	**20**	**0**	20	-	40.0	b.d.l.	10.0	10.0	40.0
	KCl	100(0)	-	100(0)	5	b.d.l.	b.d.l.	50.3(1)	49.7(1)	-
	Mgs	-	0	-	5	50.0(0)	b.d.l.	b.d.l.	b.d.l.	50.0(0)
3-2	Bulk	**70**	**0**	70	-	15.0	b.d.l.	35.0	35.0	15.0
	KCl	100(0)	-	100(0)	5	b.d.l.	b.d.l.	50.3(1)	49.7(1)	-
	Mgs	-	0	-	5	50.0(0)	b.d.l.	b.d.l.	b.d.l.	50.0(0)

Notes: #—sample number; 'Bulk'—sample bulk composition; K2# = 100·2KCl/(2KCl + $CaCO_3$ + $MgCO_3$); Ca# = 100·Ca/Ca + Mg); CO_2 = Ca + Mg + 2K − Cl_2; Cl2# = 100·Cl_2/(Cl_2 + CO_2); *n*—number of SDD-EDS analyses; standard deviations are given in brackets; '-'—not applicable or no data; '+'—phase is present.

Table 2. Phase compositions (mol%) in run D310 at 1000 °C and 24 h.

#	Phases	K2#	Ca#	Cl2#	*n*	MgO	CaO	K_2O	Cl_2	CO_2
3-5	Bulk	**20**	**100**	20	-	-	40.0	10.0	10.0	40.0
	KCl	100(0)	-	100(0)	5	b.d.l.	b.d.l.	50.2(2)	49.8(2)	-
	Cal	-	100(0)	-	5	b.d.l.	50.0(0)	b.d.l.	b.d.l.	50.0(0)
	L	56	100	56	1	b.d.l.	22.0	28.0	28.0	22.0
1-1	Bulk	**20**	**97**	20	-	1.20	38.8	10.0	10.0	40.0
	KCl	100(0)	-	100(0)	5	b.d.l.	b.d.l.	50.1(1)	49.9(1)	-
	Cal	-	98(0)	-	5	0.93(07)	49.1(1)	b.d.l.	b.d.l.	50.0(0)
	L	57(0)	93(0)	61(1)	5	1.56(3)	19.9(2)	28.2(3)	30.7(4)	19.3(4)
1-2	Bulk	**80**	**90**	80	-	1.00	9.00	40.0	40.0	10.0
	KCl	100(0)	-	100(0)	5	b.d.l.	b.d.l.	50.0(0)	50.0(1)	-
	Cal	-	98(1)	-	5	1.01(29)	49.0(5)	b.d.l.	b.d.l.	50.0(5)
	L	53(1)	90(0)	55(1)	5	2.47(9)	21.3(4)	26.3(5)	27.7(4)	22.3(4)
1-3	Bulk	**5**	**95**	5	-	2.38	45.1	2.50	2.50	47.5
	Cal	-	97(0)	-	9	1.75(15)	48.3(1)	b.d.l.	b.d.l.	50.0(0)
	L	-	-	-	+	-	-	-	-	-
4-3	Bulk	**40**	**92**	40	-	2.40	27.6	20.0	20.0	30.0
	KCl	100(0)	-	99(0)	5	b.d.l.	b.d.l.	50.2(2)	49.8(2)	b.d.l.
	Cal	-	90(2)	-	6	5.02(99)	44.8(1.0)	b.d.l.	b.d.l.	50.0(0)
	L	53(1)	83(0)	57(1)	5	3.93(8)	19.6(7)	26.4(7)	28.3(3)	21.7(3)
3-4	Bulk	**60**	**80**	60	-	4.00	16.0	30.0	30.0	20.0
	KCl	100(0)	-	100(0)	5	b.d.l.	b.d.l.	50.0(0)	50.0(1)	-
	Dol	-	76(1)	-	5	11.8(3)	38.1(4)	b.d.l.	b.d.l.	50.0(0)
	L	53(0)	78(0)	54(0)	5	5.19(13)	18.6(1)	26.3(2)	27.2(2)	22.8(2)
1-4	Bulk	**8**	**82**	8	-	8.28	37.7	4.00	4.00	46.0
	Cal	-	83(0)	-	5	8.40(22)	41.6(3)	b.d.l.	b.d.l.	50.0(1)
	L	33(1)	75(1)	35(1)	5	8.23(29)	25.1(3)	16.6(5)	17.3(4)	32.7(4)
4-1	Bulk	**57**	**75**	57	-	5.38	16.1	28.5	28.5	21.5
	KCl	100(0)	-	99(1)	5	b.d.l.	b.d.l.	50.5(5)	49.5(5)	-
	Dol	-	74(2)	-	5	13.0(1.1)	36.8(1.1)	b.d.l.	b.d.l.	50.0(0)
	L	44(1)	73(1)	45(1)	5	7.51(4)	20.7(7)	21.8(6)	22.7(5)	27.3(5)
4-2	Bulk	**7**	**62**	7	-	17.7	28.8	3.50	3.50	46.5
	Dol	-	61(1)	-	5	19.5(4)	30.5(3)	b.d.l.	b.d.l.	50.0(1)
	L	36(2)	67(1)	37(1)	5	107.(5)	21.3(4)	17.9(9)	18.5(7)	31.5(7)
2-1	Bulk	**30**	**50**	30	-	17.5	17.5	15.0	15.0	35.0
	KCl	100	-	99	3	b.d.l.	b.d.l.	50.0	50.0	-
	Dol	-	52	-	2	23.7	26.2	b.d.l.	b.d.l.	50.1
	Mgs	-	8(0)	-	5	46.2(1)	3.80(15)	b.d.l.	b.d.l.	50.0(0)
	L	40(4)	63(1)	41(4)	5	11.2(8)	18.8(1.4)	20.0(2.2)	20.3(2.2)	29.7(2.2)
2-2	Bulk	**8**	**42**	8	-	26.7	19.3	4.00	4.00	46.0
	Dol	-	50(1)	-	5	24.8(4)	25.2(4)	b.d.l.	b.d.l.	50.0(0)
	Mgs	-	7(1)	-	5	46.4(4)	3.60(40)	b.d.l.	b.d.l.	50.0(0)
	L	28(0)	61(0)	28(0)	5	14.3(0)	21.9(1)	13.8(0)	14.2(1)	35.8(1)
2-3	Bulk	**40**	**33**	40	-	20.1	9.90	20.0	20.0	30.0
	KCl	100(0)	-	99(1)	5	b.d.l.	b.d.l.	50.1(0)	49.9(3)	-
	Dol	-	51(1)	-	8	24.4(5)	25.5(7)	b.d.l.	b.d.l.	50.0(4)
	Mgs	-	8(0)	-	5	46.1(1)	3.81(13)	b.d.l.	b.d.l.	50.0(0)
	L	50	57	51	1	10.7	14.3	25.0	25.6	24.4
2-4	Bulk	**20**	**37**	20	-	25.2	14.8	10.0	10.0	40.0
	KCl	100	-	100	2	b.d.l.	b.d.l.	50.1(0)	49.9(0)	-
	Dol	-	-	-	+	-	-	-	-	-
	Mgs	-	7	-	2	46.4	3.55(34)	b.d.l.	b.d.l.	50.0
	L	42	61	42	1	11.4	17.8	20.8	21.1	28.9
4-4	Bulk	**14**	**25**	14	-	32.3	10.8	7.00	7.00	43.0
	KCl	100	-	99	1	b.d.l.	b.d.l.	50.2	49.8	-
	Dol	-	50	-	2	24.9	25.1	b.d.l.	b.d.l.	50.0
	Mgs	-	6	-	2	46.8	3.20	b.d.l.	b.d.l.	50.0
	L	40	64	40	2	10.9	19.1	20.0	20.1	29.9
3-3	Bulk	**30**	**20**	30	-	28.0	7.00	15.0	15.0	35.0
	KCl	100(0)	-	100(0)	5	b.d.l.	b.d.l.	50.0(0)	50.0(0)	-
	Dol	-	50(4)	-	5	25.2(2.2)	24.8(2.2)	b.d.l.	b.d.l.	50.0(0)
	Mgs	-	5	-	1	47.3	2.74	b.d.l.	b.d.l.	50.0
	L	48	64	51	1	9.17	16.6	24.2	25.4	24.6
3-1	Bulk	**20**	**0**	20	-	40.0	b.d.l.	10.0	10.0	40.0
	KCl	100(0)	-	99(1)	5	b.d.l.	b.d.l.	50.3(1)	49.7(3)	-
	Mgs	-	0(0)	-	5	50.0(0)	b.d.l.	b.d.l.	b.d.l.	50.0(0)
3-2	Bulk	**70**	**0**	70	-	15.0	b.d.l.	35.0	35.0	15.0
	KCl	100(0)	-	100(0)	5	b.d.l.	b.d.l.	50.0(0)	50.0(0)	-
	Mgs	-	0	-	5	50.0(0)	b.d.l.	b.d.l.	b.d.l.	50.0(0)

Notes: same as Table 1.

3. Results

The phase composition of the recovered samples and the chemical composition of phases are given in Tables 1–4. The compositions of the starting mixtures and the obtained phases are expressed as mole ratios K2# = 100·2KCl/(2KCl + $CaCO_3$ + $MgCO_3$), Ca# = 100·Ca/(Ca + Mg), and Cl2# = 100·Cl_2/(Cl_2 + CO_2). The value in brackets after the mineral symbol is the Ca#. Conventions are given in the Abbreviations section.

Table 3. Phase compositions (mol%) in run D308 at 1100 °C and 6 h.

#	Phases	K2#	Ca#	Cl2#	*n*	MgO	CaO	K_2O	Cl_2	CO_2
1-1	Bulk	**20**	**100**	20	-	-	40.0	10.0	10.0	40.0
	Cal	-	100(0)	-	5	b.d.l.	50.0(0)	b.d.l.	b.d.l.	50.0(0)
	L	50	100	50	1	b.d.l.	25.0	25.0	25.0	25.0
4-4	Bulk	**20**	**99**	20	-	0.40	39.6	10.0	10.0	40.0
	Cal	-	100(0)	-	5	b.d.l.	50.0(0)	b.d.l.	b.d.l.	50.0(0)
	L	47(1)	97(0)	47(1)	5	0.72(11)	25.9(2)	23.4(3)	23.7(3)	26.3(3)
1-2	Bulk	**80**	**100**	80	-	-	10.0	40.0	40.0	10.0
	KCl	100	-	100	2	b.d.l.	b.d.l.	50.0	50.0	-
	L	77	100	77	3	b.d.l.	11.6	38.4	38.4	11.6
4-3	Bulk	**82**	**96**	82	-	0.36	8.64	41.0	41.0	9.00
	KCl	100(0)	-	100(0)	7	b.d.l.	b.d.l.	50.4(2)	49.6(1)	-
	L	77(1)	96(1)	78(1)	5	0.49(12)	11.0(5)	38.6(6)	39.0(6)	11.0(6)
1-3	Bulk	**7**	**95**	7	-	2.33	44.2	3.50	3.50	46.5
	Cal	-	98(0)	-	5	1.14(12)	48.7(1)	b.d.l.	b.d.l.	49.8
	L	28(0)	89(0)	28(1)	5	4.00(3)	32.1(2)	13.9(2)	14.1(4)	35.9(4)
3-4	Bulk	**60**	**64**	60	-	7.20	12.8	30.0	30.0	20.0
	L	59(0)	64(0)	61(1)	5	7.29(8)	13.1(1)	29.6(1)	30.6(3)	19.4(3)
1-4	Bulk	**10**	**79**	10	-	9.45	35.6	5.00	5.00	45.0
	Cal	-	84(0)	-	5	8.19(14)	41.8(2)	b.d.l.	b.d.l.	50.0(1)
	L	21(0)	73(0)	20(0)	5	10.6(1)	28.9(2)	10.5(1)	10.1(2)	39.9(2)
4-1	Bulk	**60**	**72**	60	-	5.60	14.4	30.0	30.0	20.0
	L	59	72	61	3	5.65	14.7	29.6	30.5	19.5
2-1	Bulk	**30**	**50**	30	-	17.5	17.5	15.0	15.0	35.0
	Mgs	-	7(1)	-	6	46.4(6)	3.56(59)	b.d.l.	b.d.l.	50.0(0)
	L	32(0)	56(0)	33(0)	5	15.0(3)	18.9(0)	16.1(2)	16.4(2)	33.6(2)
2-2	Bulk	**8**	**42**	8	-	26.7	19.3	4.00	4.00	46.0
	Dol	-	48(1)	-	6	25.9(6)	24.1(4)	b.d.l.	b.d.l.	50.0(4)
	Mgs	-	9(1)	-	7	45.5(3)	4.48(26)	b.d.l.	b.d.l.	50.0(0)
	L	19(0)	58(0)	20(0)	5	17.0(1)	23.3(2)	9.74(23)	9.82(17)	40.2(2)
2-4	Bulk	**21**	**32**	21	-	26.9	12.6	10.5	10.5	39.5
	Mgs	-	7(1)	-	5	46.3(3)	3.68(28)	b.d.l.	b.d.l.	50.0(0)
	L	34(1)	55(0)	34(1)	5	14.8(3)	18.4(3)	16.8(6)	17.2(6)	32.8(6)
2-3	Bulk	**50**	**40**	50	-	15.0	10.0	25.0	25.0	25.0
	Mgs	-	4(0)	-	6	48.2(2)	1.76(21)	b.d.l.	b.d.l.	50.0(0)
	L	55(0)	49(1)	56(0)	5	11.5(3)	11.1(2)	27.3(2)	27.8(2)	22.2(2)
3-3	Bulk	**21**	**1**	21	-	39.3	0.20	10.5	10.5	39.5
	Mgs	-	0(0)	-	5	49.8(1)	0.21(7)	b.d.l.	b.d.l.	50.0(0)
	L	78(1)	6(0)	85(2)	5	10.4(7)	0.61(4)	39.0(7)	42.3(1.1)	7.7(1.1)
3-1	Bulk	**20**	**0**	20	-	40.0	0	10.0	10.0	40.0
	Mgs	-	0(0)	-	5	50.0(0)	b.d.l.	b.d.l.	b.d.l.	50.0(0)
	L	79	0	79	1	10.5	b.d.l.	39.5	39.5	10.5
4-2	Bulk	**70**	**0**	70	-	15.0	-	35.0	35.0	15.0
	KCl	100	-	100	1	b.d.l.	b.d.l.	50.0	50.0	-
	L	79	-	79	1	10.5	b.d.l.	39.5	39.5	10.5
3-2	Bulk	**79**	**5**	79	-	10.0	0.53	39.5	39.5	10.5
	L	79(1)	5(1)	83(2)	5	10.0(4)	0.54(11)	39.5(4)	41.6(8)	8.44(77)

Notes: same as Table 1.

Table 4. Phase compositions (mol%) in run D307 at 1200 °C and 3 h.

#	Phases	K2#	Ca#	Cl2#	*n*	MgO	CaO	K_2O	Cl_2	CO_2
2-1	Bulk	85	100	85	-	-	7.50	42.5	42.5	7.50
	L	85(0)	100(0)	88(1)	5	b.d.l.	7.28	42.7	44.2	5.79
2-2	Bulk	97	100	97	-	-	1.50	48.5	48.5	1.50
	KCl	100	-	100	3	b.d.l.	b.d.l.	50.0(0)	50.0(0)	-
	L	93(1)	100(0)	94(1)	5	b.d.l.	3.56(42)	46.4(4)	47.2(6)	2.75(63)
3-1	Bulk	20	0	20	-	40.0	0	10.0	10.0	40.0
	Mgs	-	0(0)	-	5	50.0(0)	b.d.l.	b.d.l.	b.d.l.	50.0(0)
	L	45(0)	1(0)	48(0)	5	27.4(1)	b.d.l.	22.6(1)	23.8(1)	26.2(1)

Notes: same as Table 1.

3.1. The System KCl–$CaCO_3$

Images of experimental samples in back-scattered electrons (BSE) are shown in Figure 1. At 900 °C (run D321, 72 h), the samples are represented by a subsolidus aggregate of $CaCO_3$ and KCl (Figure 1a,b, Table 1). At K2# 20, KCl forms grains of irregular shape up to 100 µm in size, evenly distributed in the $CaCO_3$ groundmass (Figure 1a). At K2# 80, KCl forms a groundmass while $CaCO_3$ crystals, up to 10 µm in size, appear at the KCl grain boundaries (Figure 1b).

The melting begins at 1000 °C (Run D332, 24 h). The melt layer is attached to the high-temperature (HT) capsule end. At quenching, it forms a fibrous aggregate of KCl and $CaCO_3$ (Figure 1c,e). The LT sample side consists of the subsolidus aggregate of KCl and

$CaCO_3$. At K2# 20, carbonate-chloride melt is separated from the subsolidus assemblage by the $CaCO_3$ layer (Figure 1c), while at K2# 80—by the KCl layer (Figure 1d). The melt coexisting with $CaCO_3$ at K2# 20 and KCl at K2# 80 have the same composition with K2# 56 (Figure 2, Table 2).

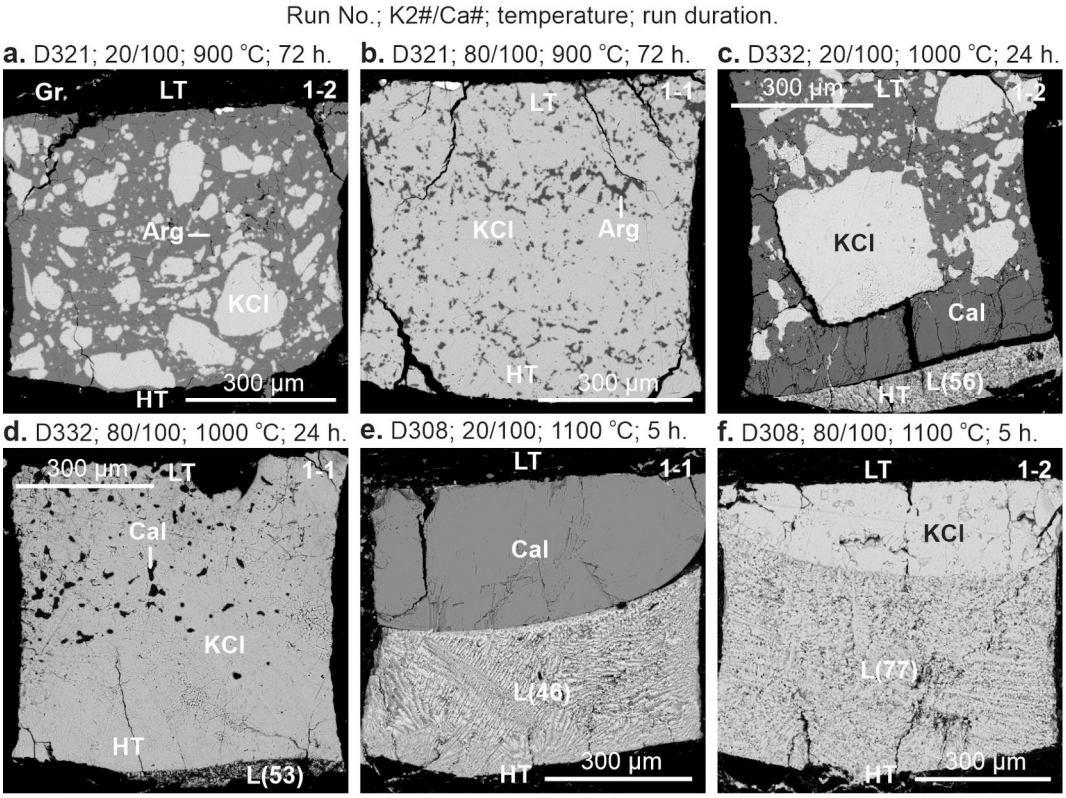

Figure 1. BSE images of sample-cross sections in the system KCl–$CaCO_3$ at 3 GPa and 900 (**a**,**b**), 1000 (**c**,**d**), and 1100 °C (**e**,**f**). The numbers in parentheses denote the melt K2#. HT—high-temperature side. LT—low-temperature side. The gravity vector is directed downward.

At 1100 °C (Run D308, 5 h) and K2# 20, almost half of the sample consists of an aggregate of 200–300 µm calcite grains and a melt pool segregated at the HT side. The quenched melt has K2# 46 and forms a mat of acicular crystals of calcite and KCl (Figure 1e). At K2# 80, about a third of the sample consists of KCl crystals 100–250 µm in size attached to the LT capsule end and melt pool at the HT side (Figure 1f). The melt has K2# 77 (Figure 2, Table 3). At K2# 70, the system undergoes complete melting.

At 1200 °C and K2# 98, 97 (Run D307, 3 h), the samples are mainly represented by crystalline KCl and a minor amount of interstitial melt with K2# 92 (Table 1). The sample with bulk K2# 85 melts completely (Figure 2, Table 4).

The obtained results are in reasonable agreement with the melting point of KCl, T_m = 1269 °C, established previously by Pistorius [39], and the melting point of $CaCO_3$, T_m = 1515 °C, determined by Shatskiy et al. [37] (Figure 2).

The Raman spectra of $CaCO_3$ correspond to aragonite at 900 °C and calcite-I ($P2_1/c$) at 1000–1200 °C. This is consistent with quenching experiments in which the calcite-aragonite transition at 3 GPa was recorded at 962 °C [40].

3.2. The System KCl–$MgCO_3$

At 900 °C (run D321, 72 h) and 1000 °C (run D310, 24 h) the samples are represented by the subsolidus assemblage of magnesite and KCl (Tables 1 and 2). Magnesite grain size varies from 5 to 60 µm, while KCl forms grains up to 160 µm in size (Figure 3a,b).

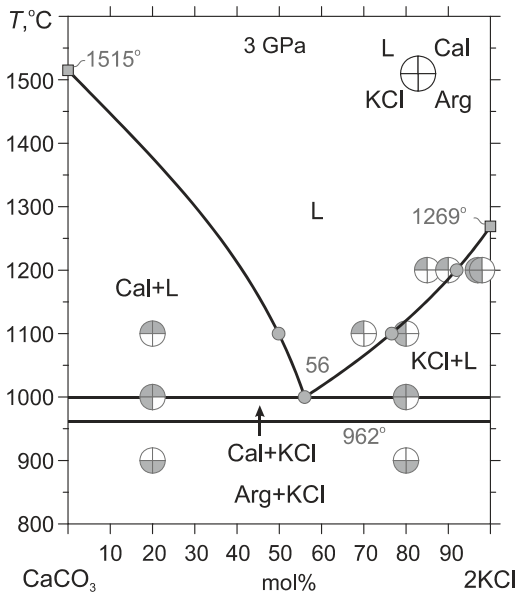

Figure 2. *T*-*X* diagram for the system KCl–$CaCO_3$ at 3 GPa. Large circles denote sample bulk composition, whereas filled segments indicate phases present. Small circles indicate the composition of melt measured by EDS. The uncertainty in the temperature estimate does not exceed the size of the small circles (≤25 °C). The $CaCO_3$ and KCl melting points are after [37,39], respectively.

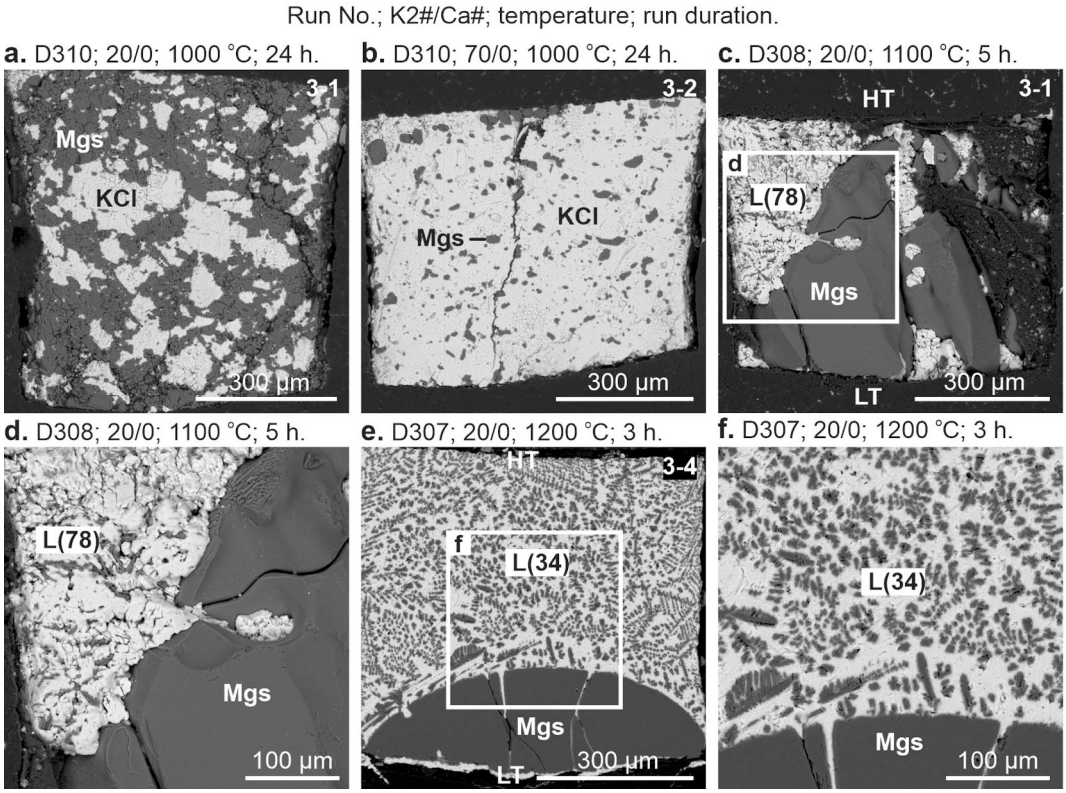

Figure 3. BSE images of sample cross-sections in the system 2KCl–$MgCO_3$ at 3 GPa and 1000 (**a**,**b**), 1100 (**c**,**d**), and 1200 °C (**e**,**f**). The numbers in parentheses denote the melt K2#. HT—high-temperature side. LT—low-temperature side. The gravity vector is directed downward.

The melting begins at 1100 °C (run D308, 5 h) (Figure 4). The melt mainly appears on the HT side, while magnesite forms large crystals, up to 400 µm, on the LT side (Figure 3c).

The melt has a chloride–carbonate composition with K2# 79 (Table 3). The melt quench products are represented by an aggregate of KCl and magnesite (Figure 3d).

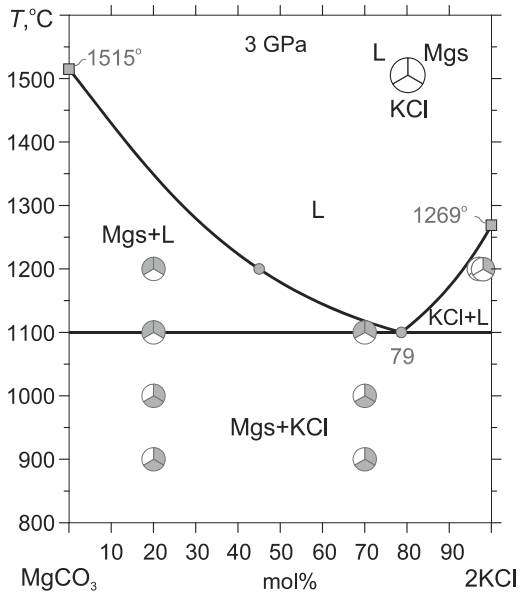

Figure 4. *T-X* diagram for the system KCl–$MgCO_3$ at 3 GPa. The $MgCO_3$ melting point is after [37]. See the caption for Figure 2 for other details.

As temperature increases to 1200 °C (run D307, 3 h), the melting degree at K2# 20 increases (Figure 3e). Magnesite forms a dome-shaped aggregate consisting of a few crystals up to 250 µm in size adjacent to the LT capsule end (Figure 3e). The melt becomes less chlorine with K2# 34 and quenches to a dendrite aggregate of magnesite and KCl (Figure 3f, Table 4).

3.3. The System KCl–$CaCO_3$–$MgCO_3$

At 900 °C, the samples are represented by a homogeneous chloride–carbonate aggregate (Figure 5a). Chloride is represented by pure KCl, while carbonates have (Ca, Mg)CO_3 composition and do not contain any K (Table 1). Carbonate is represented by calcite–dolomite solid solutions over bulk Ca# 95–75, Ca-Dol(71) + Dol(54) assemblage at bulk Ca# 60, dolomite solid solution at bulk Ca# 50–54, and Dol(50) + Mgs(1) assemblage over Ca# 25–42 (Figure 6a, Table 1).

The melting begins at 1000 °C. The melt coexists with calcite–dolomite solid solution (Figure 5c) in the range of bulk K2# $\leq$ 40 and Ca# $\geq$ 52 (Figure 6c, Table 2) and KCl at K2 $\geq$ 57 and Ca# $\geq$ 52 (Figures 5b and 6c). Subsolidus KCl + calcite–dolomite solid solution assemblage remains in the LT side of the samples with bulk K2# 40–60 (Figure 5b). The composition of the melt coexisting with calcite–dolomite solid solution ranges from K2# 58 and Ca# 95 to K2# 32–37 and Ca# 40 (Figure 6c). The composition of the melt coexisting with KCl ranges from K2#/Ca# 52/95 to 43/30 (Figure 6c, Table 2). At bulk K2#/Ca# 8/42, Mgs(7) + Dol(50) coexist with melt with K2#/Ca# 28/61 (Figures 5e and 6c). At bulk K2#/Ca# 30/20 and 40/33, Mgs(5–8) + KCl coexist with melt with K2#/Ca# 48–50/57–64 (Figures 5f and 6c). The LT side of these samples is represented by KCl + Mgs(7) + Dol(50) subsolidus assemblage (Figures 5f and 6b). At bulk K2#/Ca# 14/25, 20/37, 30/50, the samples are represented by Mgs(6–8) and liquid with K2#/Ca# 40–42/61–64 at the HT side and KCl + Dol(50–52) $\pm$ Mgs(6–7) at the LT side (Figures 5d and 6b,c, Table 2).

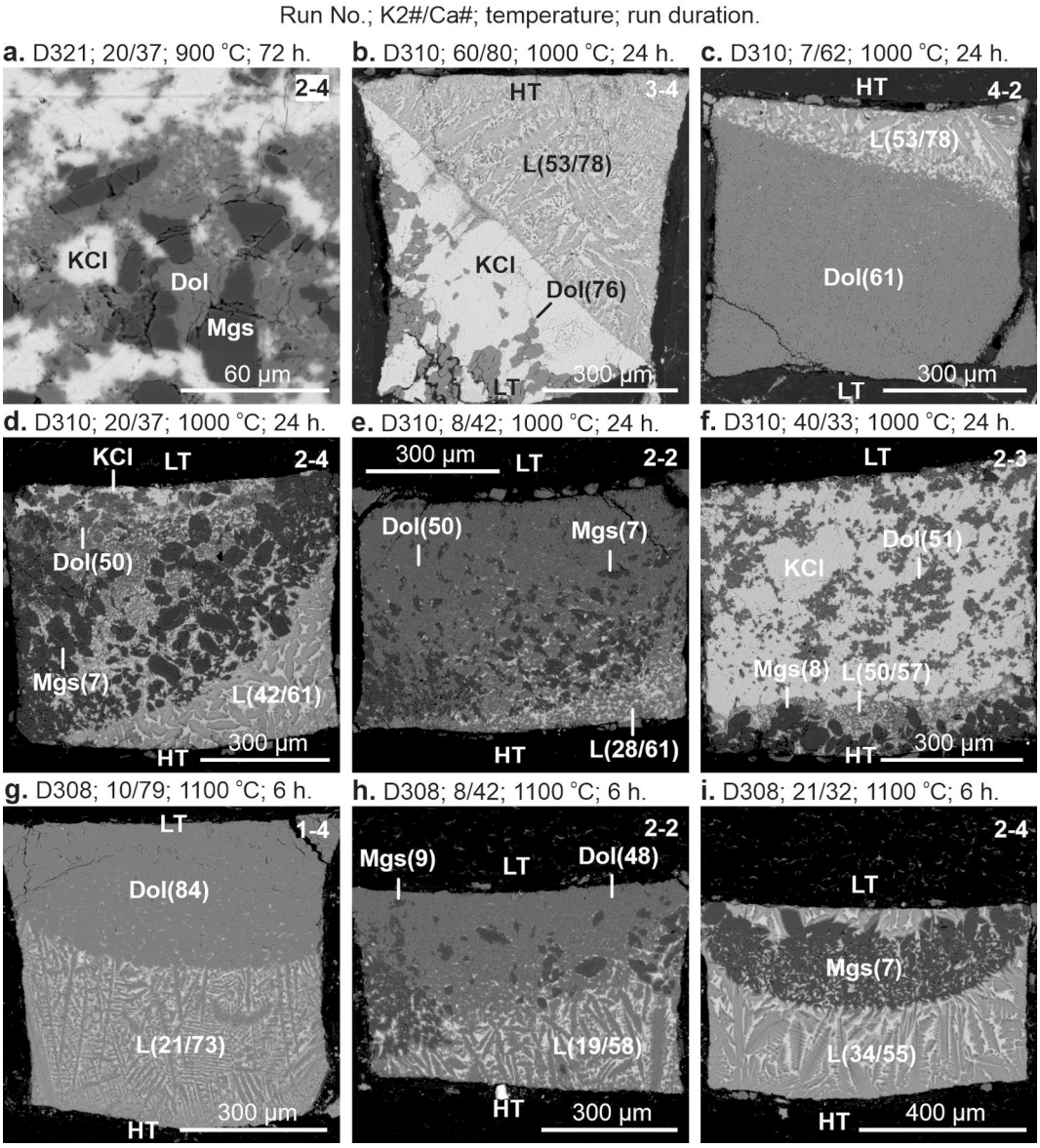

Figure 5. BSE images of sample cross-sections illustrating phase relations in the system KCl–$CaCO_3$–$MgCO_3$ at 3 GPa and 900 (**a**), 1000 (**b**–**f**), and 1100 °C (**g**–**i**). HT—high-temperature side. LT—low-temperature side. The gravity vector is directed downward. The numbers in brackets after 'Dol' and 'Mgs' are the Ca# of the corresponding phase. The numbers in brackets after 'L' are K2#/Ca#. The numbers in the upper right corner of the images are sample numbers.

As temperature increases to 1100 °C, the liquid field is getting wider, while the KCl + Mgs + Dol and KCl + Mgs fields disappear (Figure 6d). At bulk K2#/Ca# 7/95 and 10/79, calcite–dolomite solid solution coexists with liquid with K2# 21–27 and Ca# > 30 (Figures 5g and 6d, Table 3). The bulk composition with K2#/Ca# 8/42 falls in three-phase field of Mgs(9) + Dol(48) + liquid with K2#/Ca# 19/58 (Figures 5h and 6d, Table 3). The samples with Ca# < 58 and K2# < 79 fall in the field Mgs (0–9) + liquid whose composition gradually changes from K2#/Ca# 19/58 toward the binary KCl-magnesite eutectic at K2# 79 (Figure 6d). In these samples, magnesite appears as a dome-shaped aggregate of rectangular crystals 5–80 µm in size (Figure 5i). The crystals are overgrown with a shell of dolomite precipitated from the melt during quenching (Figure 5i). The melt quenches to an aggregate of dolomite forming feather-like dendrites in a KCl matrix (Figure 5i). The samples with K2#/Ca# 79/5, 60/72, and 60/64 melt completely (Figure 6d, Table 3), while samples with K2# > 78–80 consist of KCl + L (Figure 6d).

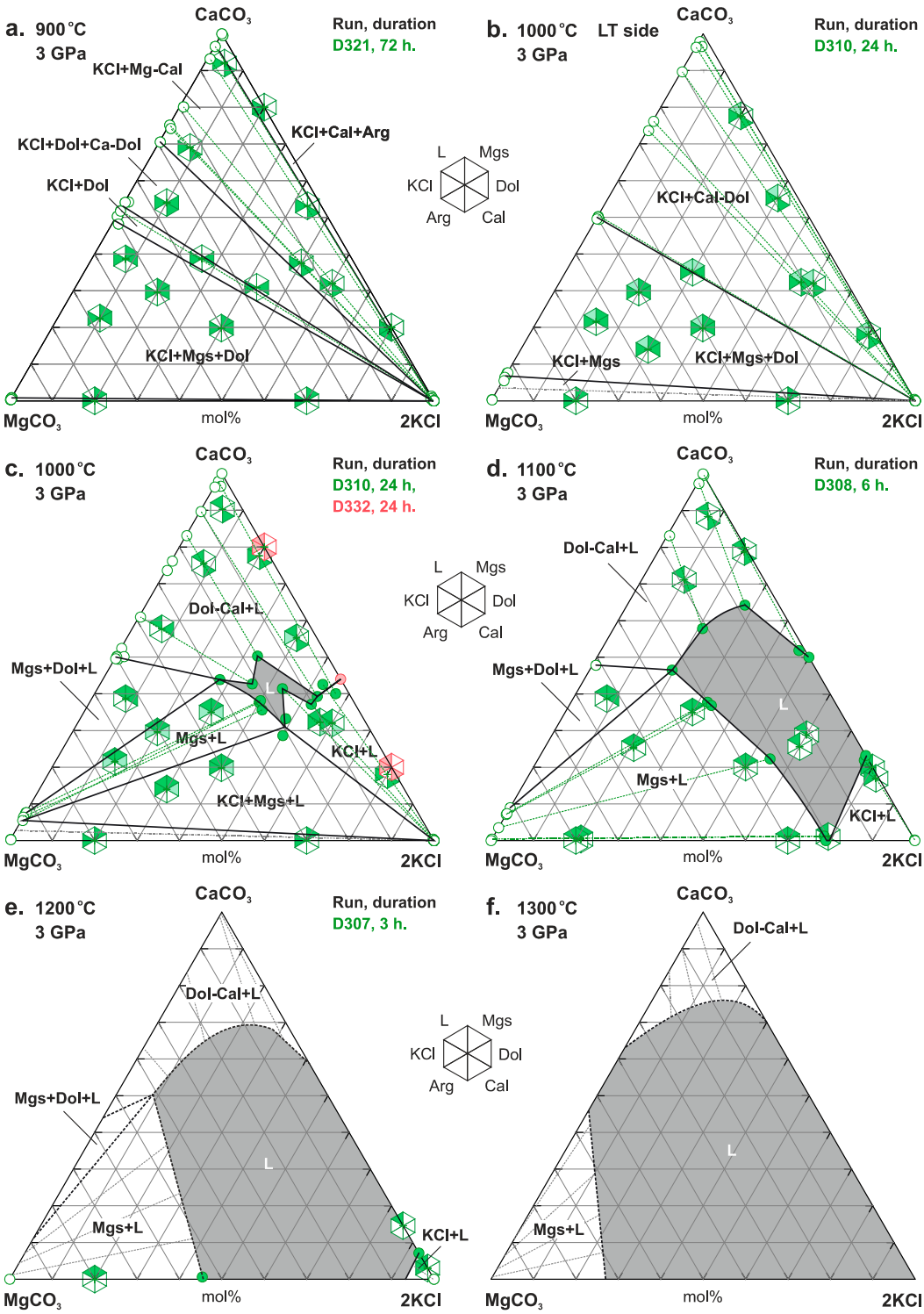

Figure 6. Isothermal sections of the KCl–$MgCO_3$–$CaCO_3$ *T*-*X* diagram at 3 GPa. (**a**) 900 °C, (**b**,**c**) 1000 °C, (**d**) 1100 °C, (**e**) 1200 °C, and (**f**) 1300 °C. Isothermal sections at 1200 and 1300 °C were constrained based on phase relations in the corresponding binaries.

Considering phase relations in the corresponding binary systems, $CaCO_3$–KCl (Figure 2), $MgCO_3$–KCl (Figure 4), and $CaCO_3$–$MgCO_3$ [37], at 1200 °C, the melt field is surrounded by three two-phase fields: KCl + L, Mgs + L, and Dol-Cal + L and one three-phase field Mgs + Dol + L (Figure 6e). At 1300 °C, KCl + L and Mgs + Dol + L fields disappear, while

Mgs + L and Dol-Cal + L fields remain up to $CaCO_3$ and $MgCO_3$ melting points established near 1515 °C at 3 GPa [37] (Figure 6f).

4. Discussion

4.1. Phase Relations in the KCl–$CaCO_3$ and KCl–$MgCO_3$ Binaries at 3 and 6 GPa

According to the present results at 3 GPa, the KCl–$CaCO_3$ system has a eutectic type of *T*-*X* diagram (Figure 7a). Below 962 °C, subsolidus assemblage is represented by KCl + aragonite, while at a higher temperature—KCl + calcite. At 1000 °C, the subsolidus KCl + calcite assemblage coexists with the chloride-carbonate melt with K2# 56 (Figure 1c). Thus, the KCl-calcite eutectic is situated at 1000 °C and has K2# 56 (Figure 2).

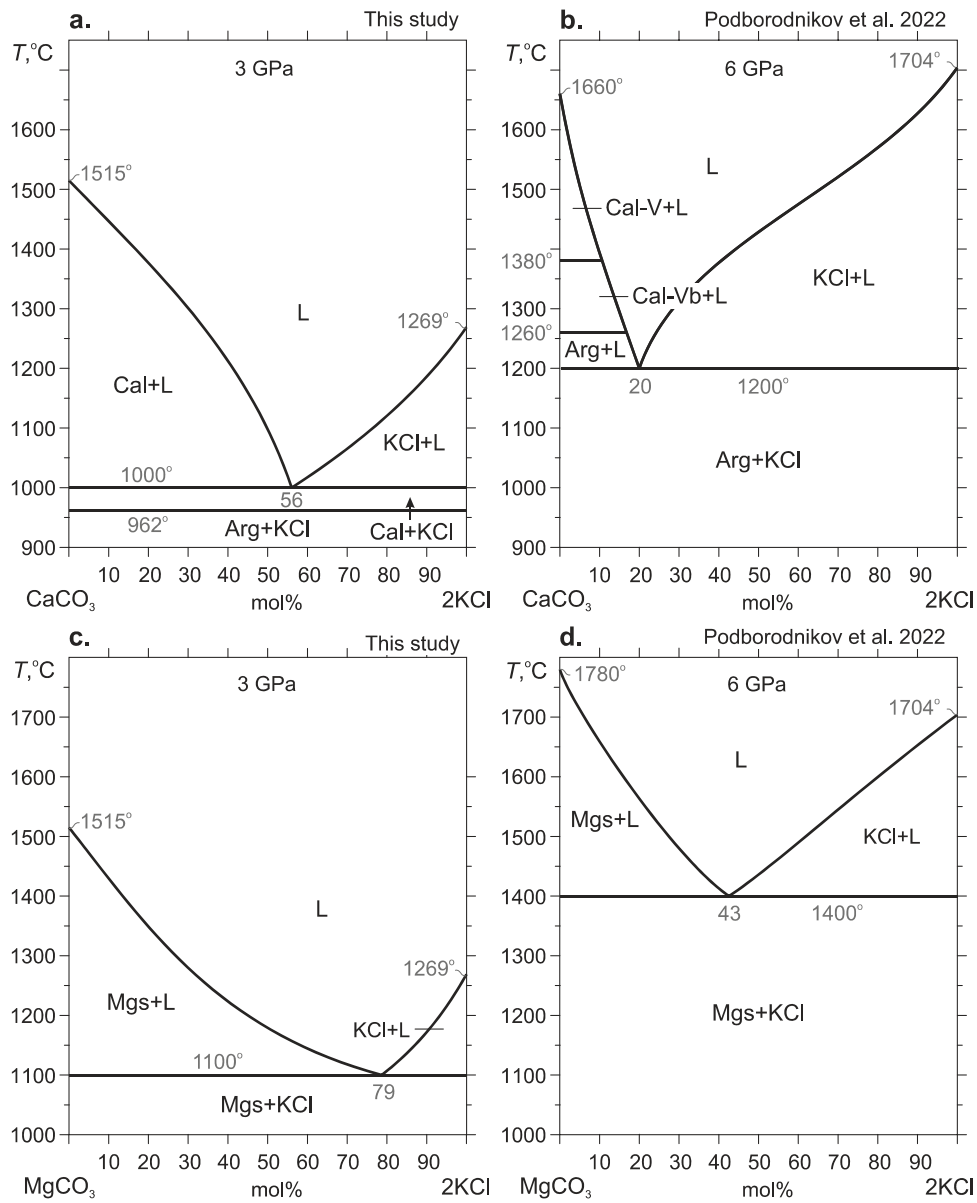

Figure 7. Comparison of binary *T*-*X* diagrams for the systems: KCl–$CaCO_3$ at 3 GPa (this study) (**a**), KCl–$CaCO_3$ at 6 GPa [33] (**b**), KCl–$MgCO_3$ at 3 GPa (this study) (**c**), KCl–$MgCO_3$ at 6 GPa [33] (**d**). According to Pistorius [41], above 1.9 GPa, KCl with the NaCl type structure (sylvite) transforms to the CsCl type structure.

At 6 GPa, the KCl–$CaCO_3$ melting is controlled by the aragonite–KCl eutectic situated at 1200 °C and K2# 20 (Figure 7b) [33]. According to in situ synchrotron radiation experi-

ments at 1260 °C aragonite transforms to calciteVb ($P2_1/m$), which is stable up to 1380 °C where it transforms to calcite-V ($R\bar{3}m$) [42] (Figure 7b). Both calcite-Vb and calcite-V are unquenchable and transform to calcite-I ($R\bar{3}c$) at atmospheric pressure [42].

At 3 and 6 GPa, the KCl–$MgCO_3$ system has a eutectic type *T*-*X* diagram (Figure 7c,d). The subsolidus assemblage is represented by KCl + magnesite. At 3 GPa, based on the liquidus extrapolation, the eutectic is located near K2# 79 and 1100 °C (Figures 4 and 7c). As pressure increases to 6 GPa, the KCl-magnesite eutectic shifts to 1400 °C and K2# 43 [33] (Figure 7d).

4.2. Phase Relations in the KCl–$CaCO_3$–$MgCO_3$ Ternary at 3 and 6 GPa

The main changes in the phase relations induced by decreasing pressure from 6 to 3 GPa result from the $CaCO_3$–$MgCO_3$ binary. At 6 GPa and 1000 °C, the system has no intermediate compounds, while at 1100 °C dolomite solid solutions with Ca# in the range 50–63 become stable. As pressure decreases to 3 GPa at 900 °C, a range of dolomite (Ca# 50–52) and calcite–dolomite (Ca# 70–97) solid solutions appear (Figure 6a). As temperature increases to 1000 °C at 3 GPa, aragonite disappears and the range of calcite–dolomite solid solutions extends to the range Ca# 50–100 (Figure 6b).

The melting phase relations at 3 GPa established in this work and at 6 GPa [32] are compared in Figure 8. At 6 GPa, the liquidus projection has seven primary solidification phase regions for KCl, magnesite, dolomite, calcite–dolomite solid solutions, calcite-V, calcite-Vb, and aragonite [32] (Figure 8b). As pressure decreases to 3 GPa, the changes in the phase relations along the $CaCO_3$–$MgCO_3$ join yield the disappearance of the primary phase regions for calcite-V, calcite-Vb, and aragonite, narrowing the primary phase field of KCl, and expansion of primary phase regions for magnesite and calcite–dolomite solid solutions (Figure 8a).

At 6 GPa, the presence of miscibility gaps between aragonite and dolomite and dolomite and magnesite splits the system into two partial ternaries: KCl + dolomite + aragonite and KCl + magnesite + dolomite. Both ternaries start to melt near 1200 °C. The melting of the first ternary is controlled by the KCl–dolomite–aragonite eutectic situated at K2#/Ca# 19/92:

$$KCl + Ca_{0.52}Mg_{0.48}CO_3\ (Dol) + CaCO_3\ (Arg) \rightarrow [30KCl{\cdot}70(Ca_{0.92}Mg_{0.18})CO_3]\ (L).\ (E\ at\ 6\ GPa)$$

The melting of the second ternary, the KCl + dolomite + magnesite assemblage, is controlled by the peritectic reaction [32] (Figure 8b):

$$KCl + CaMgCO_3\ (Dol) \rightarrow Mg_{0.89}Ca_{0.11}CO_3\ (Mgs) + [33KCl{\cdot}67(Ca_{0.69}Mg_{0.31})CO_3]\ (L).\ (P^1\ at\ 6\ GPa)$$

The resulting chloride–carbonate melt has K2#/Ca# 20/69 (Figure 8b).

As pressure decreases to 3 GPa, the KCl + dolomite + aragonite partial ternary degenerates to the binary KCl + calcite–dolomite solid solutions, while the KCl + dolomite + magnesite partial ternary remains (Figure 6b). The melting of both fields was established at 1000 °C. The minimum on the liquidus surface at K2#/Ca# 39/73 is controlled by the following eutectic reaction (Figure 8a):

$$56KCl + 44Ca_{0.73}Mg_{0.27}CO_3\ (Dol) = [56KCl{\cdot}44Ca_{0.73}Mg_{0.27}CO_3]\ (L),\quad (E\ at\ 3\ GPa)$$

wherein the Mg/Ca ratios of dolomite and melt are identical.

At bulk Ca# $\leq$ 68, the melting is controlled by peritectic at K2#/Ca# 40/68 (Figure 8a):

$$KCl + (Ca, Mg)CO_3\ (Dol) \rightarrow Mg_{0.93}Ca_{0.07}CO_3\ (Mgs) + [57KCl{\cdot}43(Ca_{0.68}Mg_{0.32})CO_3]\ (L).\ (P^1\ at\ 3\ GPa)$$

The experiments do not allow establishing the numerical difference between the temperatures of eutectic (E) and peritectic (P1) both at 3 and 6 GPa but, apparently, it does not exceed several tens of degrees. One more ternary peritectic controlled by the reaction:

$$Ca\text{-}Dol + Mgs = Dol + L,\qquad (P^2\ at\ 3\ and\ 6\ GPa)$$

is located near 1300 °C at 6 GPa and 1000 °C at 3 GPa (Figure 8).

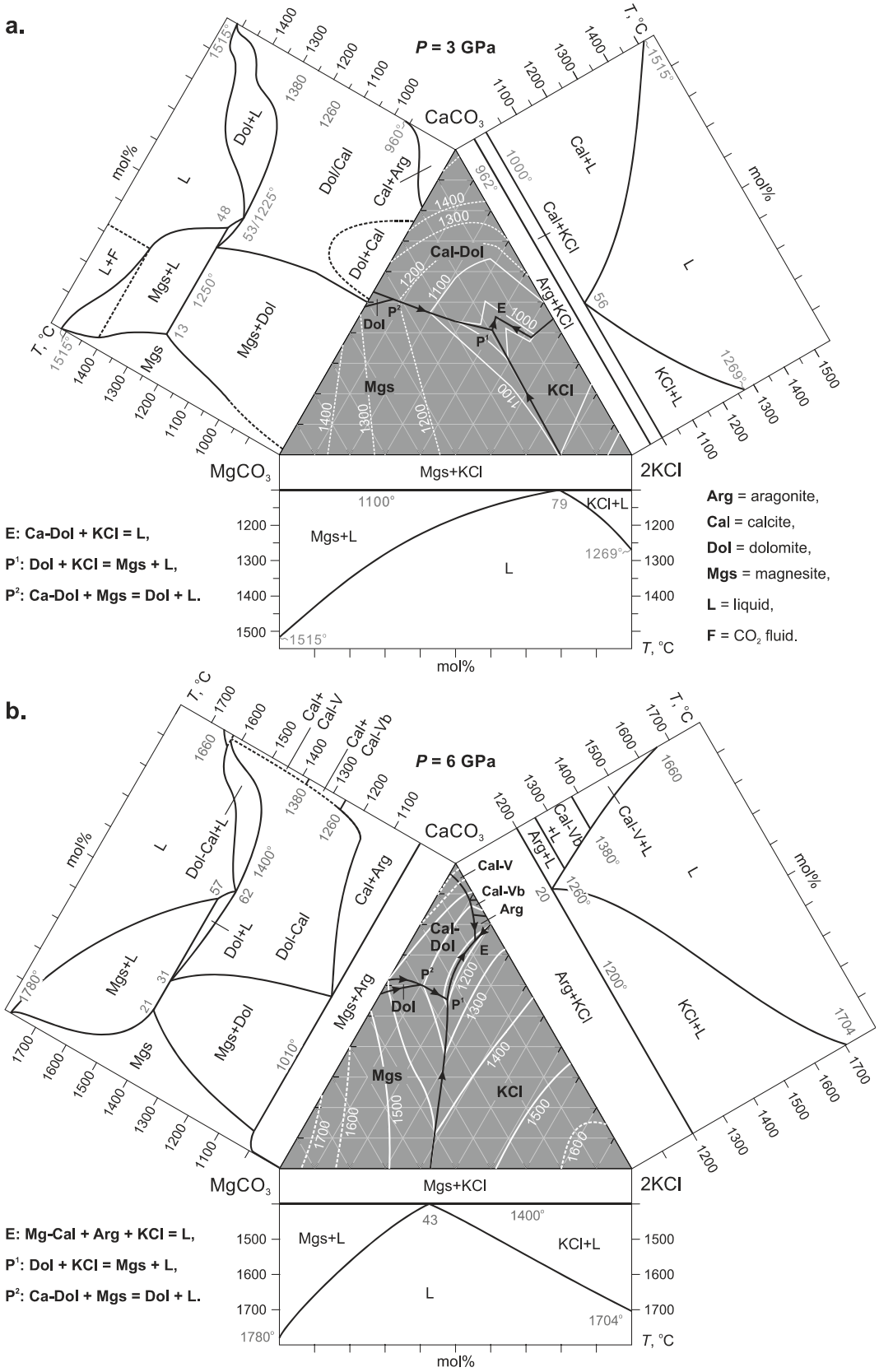

Figure 8. Isobaric equilibrium diagrams for the system KCl–$MgCO_3$–$CaCO_3$ at 3 GPa (this study) (**a**) and at 6 GPa [32,37] (**b**) Black lines are boundary lines and white lines (dashed where inferred) are liquidus isotherms with temperatures in degrees Celsius. The phase relations in the $MgCO_3$–$CaCO_3$ binary are from [37].

4.3. Comparison with the K_2CO_3–$CaCO_3$–$MgCO_3$ System

The present results coupled with data from previous studies show that the fluxing impact of potassium depends on the K host. Alkalis in pure carbonate systems enter a number of (K, Na)–(Ca, Mg, Fe) double carbonates [43–51] some of which have been found in inclusions in natural diamonds [6,8,19,52], mantle xenoliths [11,23–25,53], and kimberlite and lamproite minerals [12,13,16,17,21,22,54,55]. The studies of the K_2CO_3–$CaCO_3$–$MgCO_3$ system at 3 GPa revealed four K-bearing double carbonates including K2$(Ca_{\geq 0.84}Mg_{\leq 0.16})_2(CO_3)_3$-*R*3, $K_2(Ca_{\geq 0.70}Mg_{\leq 0.30})(CO_3)_2$-$R\bar{3}m$ buetschliite, $K_2(Mg_{\geq 0.78}Ca_{\leq 0.22})$ $(CO_3)_2$- $R\bar{3}m$, and K_2 $(Ca_{\geq 0.96}Mg_{\leq 0.04})_3(CO_3)_4$-$P2_12_12_1$ [40,56–60]. In the present study, we introduced chlorine into the K-Mg-Ca carbonate system in an amount equal to potassium (i.e., mole ratio K/Cl = 1) and found no K-bearing double carbonates as that in our recent study of the KCl–$CaCO_3$–$MgCO_3$ system at 6 GPa [32,33]. Similar behavior was observed in the case of Na in the system NaCl–$CaCO_3$–$MgCO_3$ [34,35]. Thus, the presence of double carbonates in inclusions in mantle minerals containing both chlorides and carbonates may indicate the predominance of the carbonate component over the chloride one and the bulk mole ratio K/Cl > 1. This conclusion concerns both subsolidus phases and products of melt quenching, in which dendrites of double carbonates have not been identified either.

At 3 GPa, the melting in the K_2CO_3–$CaCO_3$–$MgCO_3$ system begins at 825 °C and is controlled by K_2CO_3 + $K_2Ca(CO_3)_2$ + $K_2Mg(CO_3)_2$ eutectic situated at K2#/Ca# 53/40 [56]. Unlike that, the KCl–$CaCO_3$–$MgCO_3$ system at 3 GPa starts to melt at 1000 °C and the melting is controlled by the KCl + Ca-Dol = L eutectic at K2#/Ca# 39/73 and the KCl + Dol = Mgs + L peritectic at K2#/Ca# 40/68 (Figure 8a). Thus, replacing half of CO_3^{2-} with Cl^- in the K_2CO_3–$CaCO_3$–$MgCO_3$ system increases the solidus temperature from 825 to 1000 °C at 3 GPa and from 1050 to 1200 °C at 6 GPa and changes the incipient melt composition to less alkaline and more Ca-rich: K2#/Ca 53/40 → 39/73 at 3 GPa and 37/69 → 19/92 (Figure 9a).

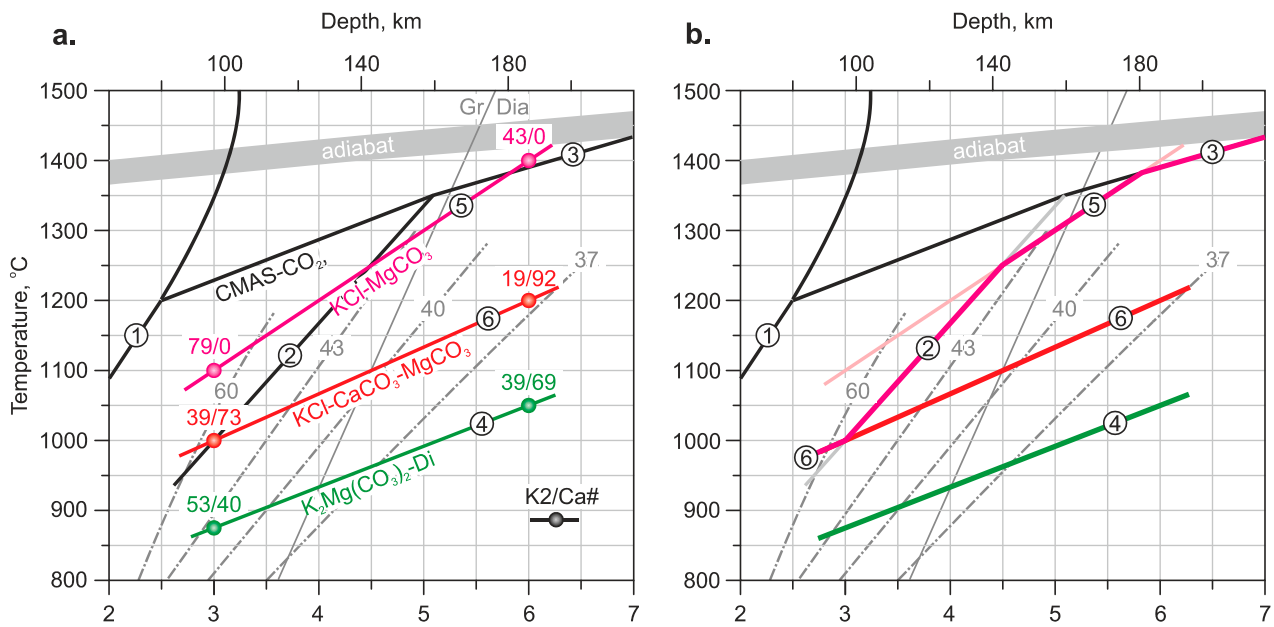

Figure 9. *Cont.*

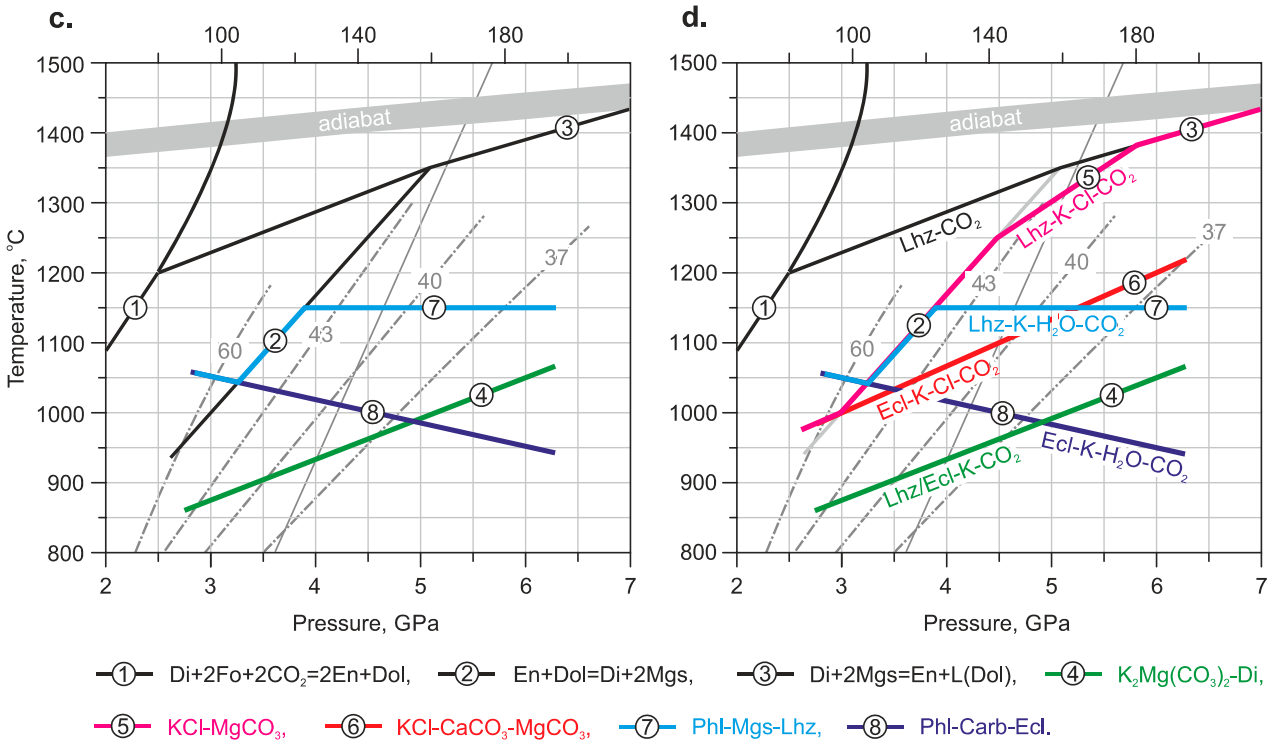

Figure 9. Solidi of K-, Cl-, and CO_2-bearing systems: (**a**) the systems KCl+$MgCO_3$, KCl+$CaCO_3$+$MgCO_3$, and diopside-$K_2Mg(CO_3)_2$; (**b**) expected solidi of the peridotite-KCl-$MgCO_3$ system (magenta) and peridotite-$K_2Mg(CO_3)_2$ system (green); (**c**) the systems carbonated phlogopite lherzolite (light blue), carbonated phlogopite eclogite (violet), diopside-$K_2Mg(CO_3)_2$ (green); (**d**) comparison of solidi of peridotite containing KCl+Mgs (magenta), Phl+Mgs (light blue), and $K_2Mg(CO_3)_2$ (green), and eclogite containing KCl+Dol (red), and Phl+Dol (violet). Dashed-dotted lines denote continental geotherms with the surface heat flow of 37, 40, 43 mW/m^2 [61]. 'adiabat'—mantle adiabat is after [62]. ①—[63,64], ②—[65], ③—[66], ④—[67], ⑤, ⑥—[32] and this study, ⑦—[68], ⑧—[69].

4.4. Implications for Peridotite and Eclogite Solidi

The CaO-MgO-Al_2O_3-SiO_2-CO_2 (CMAS-CO_2) system is the base for studying phase relationships in mantle suits in presence of CO_2. In the case of lherzolite, the increase in pressure is accompanied by a carbonation reaction [63,64]:

$$CaMgSi_2O_6\ (Di) + Mg_2SiO_4\ (Fo) + 2CO_2\ (F) = 2Mg_2Si_2O_6\ (En) + CaMg(CO_3)_2\ (Dol), \quad (1)$$

which takes place at a pressure of 1.5–2.5 GPa (Figure 9a). Stabilization of dolomite leads to a sharp decrease in the solidus to 1200 °C at 2.5 GPa (Figure 9a) [70]. A further increase in pressure is accompanied by the Ca–Mg exchange reaction [65]:

$$Mg_2Si_2O_6\ (En) + CaMg(CO_3)_2\ (Dol) = CaMgSi_2O_6\ (Di) + 2MgCO_3\ (Mgs). \quad (2)$$

Reaction (2) stabilizes the clinopyroxene + magnesite assemblage, which controls the lherzolite solidus in the CMAS-CO_2 system at pressures exceeding 5 GPa [66] (Figure 9a):

$$CaMgSi_2O_6\ (Di) + 2MgCO_3\ (Mgs) = Mg_2Si_2O_6\ (En) + CaMg(CO_3)_2\ (L). \quad (3)$$

It was shown that potassium significantly (by 350–400 °C) lowers this solidus [71–73]. This occurs due to the stabilization of $K_2Mg(CO_3)_2$, which participates in the melting reaction, lowering the solidus temperature to 1050 °C at 6 GPa [74] (Figure 9a):

$$CaMgSi_2O_6\ (Di) + 2K_2Mg(CO_3)_2\ (Eit) = Mg_2Si_2O_6\ (En) + [2K_2CO_3 + CaCO_3 + MgCO_3]\ (L). \quad (4)$$

Note that $K_2Mg(CO_3)_2$ was found as mineral inclusions in natural diamonds [8].

Recently we showed that the partial replacement of CO_3^{2-} with Cl^- stabilizes the KCl + $MgCO_3$ assemblage instead of $K_2Mg(CO_3)_2$ [32,33]. It should be noted that the KCl found in inclusions in diamonds appears in touch with magnesite [6]. The melting of the KCl + $MgCO_3$ assemblage is controlled by the eutectic situated at 1400 °C at 6 GPa (Figures 8b and 9a). Thus, the addition of chlorine in an amount identical to the amount of potassium should raise the solidus temperature of the lherzolite-CO_2 system to that of CMAS-CO_2 [66] (the magenta line in Figure 9b). Below 6 GPa the KCl-$MgCO_3$ solidus becomes cooler than that of CMAS-CO_2 (Figure 9a). Therefore, in the pressure range of 4.5–5.8 GPa, the solidus of the lherzolite–Mgs–KCl system would be controlled by the melting of the KCl + magnesite assemblage (Figure 9b):

$$\text{KCl (solid)} + \text{MgCO}_3\text{ (Mgs)} \rightarrow [\text{KCl} + \text{MgCO}_3]\text{ (L)}. \quad (5)$$

At 4.5 GPa and 1250 °C, reaction (5) crossovers reaction (2) stabilizing dolomite. Stabilization of dolomite in presence of KCl should yield melting along line (2) in the range from 4.5 GPa/1250 °C to 3 GPa/1000 °C, where reaction (2) crossover the KCl–$CaCO_3$–$MgCO_3$ solidus (Figure 9b). We expect that at a pressure $\leq$ 3 GPa, the KCl-bearing carbonated lherzolite solidus would be controlled by the melting of the KCl + dolomite assemblage (line (6) in Figure 9b).

We also expect that solidus of KCl-bearing carbonated eclogite in the range 3–6 GPa will be controlled by melting phase relations in the KCl–$CaCO_3$–$MgCO_3$ system, namely, by the peritectic reaction (red line (6) in Figure 9b):

$$\text{KCl} + \text{CaMgCO}_3\text{ (Dol)} \rightarrow \text{MgCO}_3\text{ (Mgs)} + \text{(L)}, \quad (6)$$

which is located 150 °C higher than reaction (4) controlling the carbonated eclogite solidus (the green line in Figure 9b). As can be seen, the inhibition of chlorine, if it yields replacement of K_2CO_3 with KCl, on the fluxing effect of potassium on carbonated eclogite solidus would be twice lower than that in the case of carbonated lherzolite at 6 GPa and becomes the same at 3 GPa owing to the stabilization of dolomite in the ultramafic system (Figure 9d). It is interesting to note that KCl in association with dolomite and magnesite has been found as inclusions in diamonds [6,18].

The inhibition of H_2O on the fluxing effect of potassium in carbonated lherzolite was also revealed [68]. Water stabilizes phlogopite instead of $K_2Mg(CO_3)_2$. The phlogopite + magnesite + clinopyroxene assemblage is more refractory than $K_2Mg(CO_3)_2$ + clinopyroxene [67,75], as a result, the solidus temperature of K-bearing carbonated peridotite increases to 1200 °C at 4–6 GPa [68] (Figure 9c):

$$2\text{KMg}_3\text{AlSi}_3\text{O}_{10}(\text{OH})_2\text{ (Phl)} + \text{CaMgSi}_2\text{O}_6\text{ (Cpx)} + 3\text{MgCO}_3\text{ (Mgs)} = \text{Mg}_3\text{Al}_2\text{Si}_3\text{O}_{12}\text{ (Grt)} +$$
$$2\text{Mg}_2\text{Si}_2\text{O}_6\text{ (Opx)} + \text{Mg}_2\text{SiO}_4\text{ (Ol)} + [\text{K}_2\text{CO}_3 + \text{CaMg(CO}_3)_2 + 2\text{H}_2\text{O}]\text{ (L)}. \quad (7)$$

At 6 GPa, the position of the carbonated phlogopite lherzolite solidus is 250 °C cooler than that expected for KCl-bearing carbonated lherzolite (Figure 9d) [32]. Below 4 GPa both solidi would coincide with the boundary of reaction (2), and at 3 GPa the solidus of the KCl-bearing lherzolite would be 50 °C cooler (Figure 9d). The results in the KCl–$CaCO_3$–$MgCO_3$ system indicate that the inhibition of chlorine, if it yields replacement of K_2CO_3 with KCl, on the fluxing effect of potassium on peridotite solidus would be twice stronger than water at 6 GPa and becomes comparable with that of water near 3 GPa (Figure 9d). However, this assumption and the integral effects of water and chlorine (chlorides) have yet to be elucidated.

The carbonated phlogopite eclogite solidus is situated 100 °C lower than reaction (4) controlling solidus of K-rich carbonated eclogite under anhydrous conditions and 250 °C lower than the solidus of the KCl–$CaCO_3$–$MgCO_3$ system (line (6) in Figure 9d). However, as pressure decreases carbonated phlogopite solidus crossovers reaction (4) at 5 GPa and

reaction (6) at 3.5 GPa, and becomes 50 and 175 °C higher than reactions expected to be control solidi of KCl-bearing carbonated eclogite and $K_2Mg(CO_3)_2$-bearing eclogite, respectively (Figure 9d).

5. Conclusions

Based on the results of multianvil experiments at 3 GPa in the KCl–$CaCO_3$–$MgCO_3$ system the following conclusions can be drawn:

1. The KCl–$CaCO_3$ binary has eutectic type *T*-*X* diagrams. At 900 °C, the subsolidus assemblage is represented by KCl + aragonite, while at 1000 °C by KCl + calcite. The KCl–calcite eutectic is situated at 1000 °C and K2# 56, where K2# = 2KCl/(2KCl + $CaCO_3$ + $MgCO_3$) × 100 mol%. The KCl–$MgCO_3$ binary has eutectic type *T*-*X* diagrams. At 900–1000 °C, the subsolidus assemblage is represented by KCl + magnesite. The KCl-magnesite eutectic is situated at 1100 °C and K2# 79.
2. In the KCl–$CaCO_3$–$MgCO_3$ ternary subsolidus assemblage consists of KCl and Ca-Mg carbonates. Just below solidus, the system is divided into two partial ternaries: KCl + magnesite + dolomite and KCl + calcite–dolomite solid solutions. The melting of both partial ternaries was established at 1000 °C. The system has one eutectic situated at K2#/Ca# 39/73 and two peritectics: KCl + dolomite = magnesite + liquid at K2#/Ca# 40/68 and Ca-dolomite + magnesite = dolomite + liquid, where Ca# = 100·Ca/(Ca + Mg) × 100 mol%.

Author Contributions: Conceptualization, A.S.; methodology, A.S. and K.D.L.; validation, K.D.L.; formal analysis, I.V.P., A.V.A. and A.S.; investigation, I.V.P.; resources, A.S. and K.D.L.; data curation, I.V.P. and A.S.; writing—original draft preparation, A.S.; writing—review and editing, A.S.; visualization, I.V.P. and A.S.; supervision, A.S.; project administration, A.S.; funding acquisition, A.S. All authors have read and agreed to the published version of the manuscript.

Funding: This research was funded by Russian Science Foundation (project No 21-17-00024).

Acknowledgments: We are grateful to V.G. Butvina and two anonymous reviewers for constructive reviews; N.S. Karmanov, A.T. Titov, and M.V. Khlestov for assistance in the analytical works.

Conflicts of Interest: The authors declare no conflict of interest.

Abbreviations

Arg—aragonite, Cal—calcite, Ca-Dol—calcium dolomite, Cal-Dol—calcite–dolomite solid solutions, Cal-V—calcite-V ($R\bar{3}m$), Cal-Vb—calcite-Vb ($P2_1/m$), Dol—dolomite, Mag—magnesite, Mg-Cal—magnesian calcite, L—liquid, Ca# = 100·Ca/(Ca + Mg)×100 mol%, K2# = 2KCl/(2KCl + $CaCO_3$ + $MgCO_3$) × 100 mol%, Cl2# = Cl_2/(Cl_2 + CO_2) × 100 mol%, HT—high temperature, LT—low temperature. The value in brackets after the mineral symbol is the Ca#, Dol(), Cal(), Mgs().

References

1. Navon, O.; Hutcheon, I.; Rossman, G.; Wasserburg, G. Mantle-derived fluids in diamond micro-inclusions. *Nature* **1988**, *335*, 784–789. [CrossRef]
2. Izraeli, E.S.; Harris, J.W.; Navon, O. Brine inclusions in diamonds: A new upper mantle fluid. *Earth Planet. Sci. Lett.* **2001**, *187*, 323–332. [CrossRef]
3. Klein-BenDavid, O.; Izraeli, E.S.; Hauri, E.; Navon, O. Fluid inclusions in diamonds from the Diavik mine, Canada and the evolution of diamond-forming fluids. *Geochim. Cosmochim. Acta* **2007**, *71*, 723–744. [CrossRef]
4. Logvinova, A.M.; Wirth, R.; Fedorova, E.N.; Sobolev, N.V. Nanometre-sized mineral and fluid inclusions in cloudy Siberian diamonds: New insights on diamond formation. *Eur. J. Mineral.* **2008**, *20*, 317–331.
5. Kamenetsky, V.S.; Maas, R.; Kamenetsky, M.B.; Paton, C.; Phillips, D.; Golovin, A.V.; Gornova, M.A. Chlorine from the mantle: Magmatic halides in the Udachnaya-East kimberlite, Siberia. *Earth Planet. Sci. Lett.* **2009**, *285*, 96–104. [CrossRef]
6. Kaminsky, F.V.; Wirth, R.; Schreiber, A. Carbonatitic inclusions in deep mantle diamond from Juina, Brazil: New minerals in the carbonate-halide association. *Can. Mineral.* **2013**, *51*, 669–688. [CrossRef]

7. Weiss, Y.; McNeill, J.; Pearson, D.G.; Nowell, G.M.; Ottley, C.J. Highly saline fluids from a subducting slab as the source for fluid-rich diamonds. *Nature* **2015**, *524*, 339–342.
8. Jablon, B.M.; Navon, O. Most diamonds were created equal. *Earth Planet. Sci. Lett.* **2016**, *443*, 41–47. [CrossRef]
9. Zedgenizov, D.A.; Ragozin, A.L.; Shatsky, V.S.; Griffin, W.L. Diamond formation during metasomatism of mantle eclogite by chloride-carbonate melt. *Contrib. Mineral. Petrol.* **2018**, *173*, 84.
10. Weiss, Y.; Czas, J.; Navon, O. Fluid inclusions in fibrous diamonds. *Rev. Mineral. Geochem.* **2022**, *88*, 475–532.
11. Sharygin, I.S.; Golovin, A.V.; Tarasov, A.A.; Dymshits, A.M.; Kovaleva, E. Confocal Raman spectroscopic study of melt inclusions in olivine of mantle xenoliths from the Bultfontein kimberlite pipe (Kimberley cluster, South Africa): Evidence for alkali-rich carbonate melt in the mantle beneath Kaapvaal Craton. *J. Raman Spectrosc.* **2021**, *53*, 508–524. [CrossRef]
12. Abersteiner, A.; Golovin, A.; Chayka, I.; Kamenetsky, V.S.; Goemann, K.; Rodemann, T.; Ehrig, K. Carbon Compounds in the West Kimberley Lamproites (Australia): Insights from Melt and Fluid Inclusions. *Gondwana Res.* **2022**, *109*, 536–557. [CrossRef]
13. Abersteiner, A.; Giuliani, A.; Kamenetsky, V.S.; Phillips, D. Petrographic and melt-inclusion constraints on the petrogenesis of a magmaclast from the Venetia kimberlite cluster, South Africa. *Chem. Geol.* **2017**, *455*, 331–341. [CrossRef]
14. Kopylova, M.; Navon, O.; Dubrovinsky, L.; Khachatryan, G. Carbonatitic mineralogy of natural diamond-forming fluids. *Earth Planet. Sci. Lett.* **2010**, *291*, 126–137. [CrossRef]
15. Izraeli, E.S.; Harris, J.W.; Navon, O. Fluid and mineral inclusions in cloudy diamonds from Koffiefontein, South Africa. *Geochim. Et Cosmochim. Acta* **2004**, *68*, 2561–2575. [CrossRef]
16. Golovin, A.V.; Sharygin, V.V.; Pokhilenko, N.P.; Mal'kovets, V.G.; Kolesov, B.A.; Sobolev, N.V. Secondary melt inclusions in olivine from unaltered kimberlites of the Udachnaya-East pipe, Yakutia. *Dokl. Earth Sci.* **2003**, *388*, 93–96.
17. Tarasov, A.A.; Golovin, A.V.; Sharygin, I.S. Alkali-containing minerals within melt inclusions in olivine of mantle xenoliths from bultfontein kimberlite pipe (Kaapvaal craton): Evidence on high concentrations of alkalis in kimberlite melts. *Geodyn. Tectonophys.* **2022**, *13*, 0662. [CrossRef]
18. Kaminsky, F.V.; Ryabchikov, I.D.; Wirth, R. A primary natrocarbonatitic association in the Deep Earth. *Mineral. Petrol.* **2016**, *110*, 387–398. [CrossRef]
19. Kaminsky, F.; Wirth, R.; Matsyuk, S.; Schreiber, A.; Thomas, R. Nyerereite and nahcolite inclusions in diamond: Evidence for lower-mantle carbonatitic magmas. *Mineral. Mag.* **2009**, *73*, 797–816. [CrossRef]
20. Palyanov, Y.N.; Sokol, A.G. The effect of composition of mantle fluids/melts on diamond formation processes. *Lithos* **2009**, *112*, 690–700. [CrossRef]
21. Kamenetsky, M.B.; Sobolev, A.V.; Kamenetsky, V.S.; Maas, R.; Danyushevsky, L.V.; Thomas, R.; Pokhilenko, N.P.; Sobolev, N.V. Kimberlite melts rich in alkali chlorides and carbonates: A potent metasomatic agent in the mantle. *Geology* **2004**, *32*, 845–848. [CrossRef]
22. Kamenetsky, V.S.; Golovin, A.V.; Maas, R.; Giuliani, A.; Kamenetsky, M.B.; Weiss, Y. Towards a new model for kimberlite petrogenesis: Evidence from unaltered kimberlites and mantle minerals. *Earth-Sci. Rev.* **2014**, *139*, 145–167.
23. Golovin, A.V.; Sharygin, I.S.; Korsakov, A.V.; Kamenetsky, V.S.; Abersteiner, A. Can primitive kimberlite melts be alkali-carbonate liquids: Composition of the melt snapshots preserved in deepest mantle xenoliths. *J. Raman Spectrosc.* **2020**, *51*, 1849–1867. [CrossRef]
24. Giuliani, A.; Kamenetsky, V.S.; Phillips, D.; Kendrick, M.A.; Wyatt, B.A.; Goemann, K. Nature of alkali-carbonate fluids in the sub-continental lithospheric mantle. *Geology* **2012**, *40*, 967–970. [CrossRef]
25. Golovin, A.; Sharygin, I.; Kamenetsky, V.; Korsakov, A.; Yaxley, G. Alkali-carbonate melts from the base of cratonic lithospheric mantle: Links to kimberlites. *Chem. Geol.* **2018**, *483*, 261–274. [CrossRef]
26. Safonov, O.G.; Perchuk, L.L.; Litvin, Y.A. Melting relations in the chloride-carbonate-silicate systems at high-pressure and the model for formation of alkalic diamond-forming liquids in the upper mantle. *Earth Planet. Sci. Lett.* **2007**, *253*, 112–128. [CrossRef]
27. Butvina, V.G.; Safonov, O.G.; Litvin, Y.A. Experimental study of eclogite melting with participation of the H_2O-CO_2-KCl fluid at 5 GPa. *Dokl. Earth Sci.* **2009**, *427*, 956–960.
28. Safonov, O.G.; Chertkova, N.V.; Perchuk, L.L.; Litvin, Y.A. Experimental model for alkalic chloride-rich liquids in the upper mantle. *Lithos* **2009**, *112*, 260–273. [CrossRef]
29. Safonov, O.G.; Perchuk, L.L.; Yapaskurt, V.O.; Litvin, Y.A. Immiscibility of carbonate-silicate and chloride-carbonate melts in the kimberlite-$CaCO_3$–Na_2CO_3–KCl system at 4.8 GPa. *Dokl. Earth Sci.* **2009**, *424*, 388–392. [CrossRef]
30. Litasov, K.D.; Safonov, O.G.; Ohtani, E. Origin of Cl-bearing silica-rich melt inclusions in diamonds: Experimental evidence for an eclogite connection. *Geology* **2010**, *38*, 1131–1134. [CrossRef]
31. Litasov, K.D.; Sharygin, I.S.; Shatskiy, A.F.; Ohtani, E.; Pokhilenko, N.P. Experimental constraints on the role of chloride in the origin and evolution of kimberlitic magma. *Dokl. Earth Sci.* **2010**, *435*, 1641–1646. [CrossRef]
32. Shatskiy, A.; Podborodnikov, I.V.; Arefiev, A.V.; Bekhtenova, A.; Litasov, K.D. The KCl−$CaCO_3$−$MgCO_3$ system at 6 GPa: A link between saline and carbonatitic diamond-forming fluids. *Chem. Geol.* **2022**, *604*, 120931. [CrossRef]
33. Podborodnikov, I.V.; Shatskiy, A.; Arefiev, A.V.; Bekhtenova, A.; Litasov, K.D. The systems KCl–$CaCO_3$ and KCl–$MgCO_3$ at 6 GPa. *High Press. Res.* **2022**, *42*, 245–258. [CrossRef]
34. Shatskiy, A.; Podborodnikov, I.V.; Fedoraeva, A.S.; Arefiev, A.V.; Bekhtenova, A.; Litasov, K.D. The NaCl-$CaCO_3$ and NaCl-$MgCO_3$ systems at 6 GPa: Link between saline and carbonatitic diamond forming melts. *Am. Mineral.* 2023; *in press*. [CrossRef]

35. Shatskiy, A.; Podborodnikov, I.V.; Arefiev, A.V.; Bekhtenova, A.; Litasov, K.D. Genetic link between saline and carbonatitic mantle fluids: The system NaCl-$CaCO_3$-$MgCO_3$±H_2O±Fe^0 at 6 GPa. *Geosci. Front.* **2022**, *13*, 101431. [CrossRef]
36. Shatskiy, A.; Litasov, K.D.; Terasaki, H.; Katsura, T.; Ohtani, E. Performance of semi-sintered ceramics as pressure-transmitting media up to 30 GPa. *High Press. Res.* **2010**, *30*, 443–450. [CrossRef]
37. Shatskiy, A.; Podborodnikov, I.V.; Arefiev, A.V.; Minin, D.A.; Chanyshev, A.D.; Litasov, K.D. Revision of the $CaCO_3$–$MgCO_3$ phase diagram at 3 and 6 GPa. *Am. Mineral.* **2018**, *103*, 441–452. [CrossRef]
38. Lavrent'ev, Y.G.; Karmanov, N.S.; Usova, L.V. Electron probe microanalysis of minerals: Microanalyzer or scanning electron microscope? *Russ. Geol. Geophys.* **2015**, *56*, 1154–1161. [CrossRef]
39. Pistorius, C.W.F.T. Melting curves of the potassium halides at high pressures. *J. Phys. Chem. Solids* **1965**, *26*, 1543–1548.
40. Arefiev, A.V.; Shatskiy, A.; Podborodnikov, I.V.; Rashchenko, S.V.; Chanyshev, A.D.; Litasov, K.D. The system K_2CO_3-$CaCO_3$ at 3 GPa: Link between phase relations and variety of K-Ca double carbonates at $\leq$ 0.1 and 6 GPa. *Phys. Chem. Miner.* **2019**, *46*, 229–244. [CrossRef]
41. Pistorius, C.W.F.T. Polymorphic transitions of the alkali chlorides at high pressures to 200 °C. *J. Phys. Chem. Solids* **1964**, *25*, 1477–1481. [CrossRef]
42. Druzhbin, D.; Rashchenko, S.; Shatskiy, A.; Crichton, W. New high-pressure, high-temperature $CaCO_3$ polymorph. *ACS Earth Space Chem.* **2022**, *6*, 1506–1513. [CrossRef]
43. Niggli, P. Gleichgewichte zwischen TiO_2 und CO_2, sowie SiO_2 und CO_2 in Alkali-, Kalk-Alkali und Alkali-Aluminatschmelzen. *Z. Anorg. Und Allg. Chem.* **1916**, *98*, 241–326. [CrossRef]
44. Eitel, W.; Skaliks, W. Some double carbonates of alkali and earth alkali. *Z. Anorg. Und Allg. Chem.* **1929**, *183*, 263–286. [CrossRef]
45. Cooper, A.F.; Gittins, J.; Tuttle, O.F. The system Na_2CO_3–K_2CO_3–$CaCO_3$ at 1 kilobar and its significance in carbonatite petrogenesis. *Am. J. Sci.* **1975**, *275*, 534–560. [CrossRef]
46. Shatskiy, A.; Sharygin, I.S.; Gavryushkin, P.N.; Litasov, K.D.; Borzdov, Y.M.; Shcherbakova, A.V.; Higo, Y.; Funakoshi, K.-i.; Palyanov, Y.N.; Ohtani, E. The system K_2CO_3-$MgCO_3$ at 6 GPa and 900–1450 °C. *Am. Mineral.* **2013**, *98*, 1593–1603. [CrossRef]
47. Shatskiy, A.; Sharygin, I.S.; Litasov, K.D.; Borzdov, Y.M.; Palyanov, Y.N.; Ohtani, E. New experimental data on phase relations for the system Na_2CO_3–$CaCO_3$ at 6 GPa and 900–1400 °C. *Am. Mineral.* **2013**, *98*, 2164–2171. [CrossRef]
48. Shatskiy, A.; Borzdov, Y.M.; Litasov, K.D.; Sharygin, I.S.; Palyanov, Y.N.; Ohtani, E. Phase relationships in the system K_2CO_3-$CaCO_3$ at 6 GPa and 900–1450 °C. *Am. Mineral.* **2015**, *100*, 223–232. [CrossRef]
49. Podborodnikov, I.V.; Shatskiy, A.; Arefiev, A.V.; Litasov, K.D. Phase relations in the system Na_2CO_3–$CaCO_3$–$MgCO_3$ at 3 GPa with implications for carbonatite genesis and evolution. *Lithos* **2019**, *330–331*, 74–89. [CrossRef]
50. Arefiev, A.V.; Shatskiy, A.; Podborodnikov, I.V.; Litasov, K.D. The K_2CO_3–$CaCO_3$–$MgCO_3$ system at 6 GPa: Implications for diamond forming carbonatitic melts. *Minerals* **2019**, *9*, 558. [CrossRef]
51. Podborodnikov, I.V.; Shatskiy, A.; Arefiev, A.V.; Bekhtenova, A.; Litasov, K.D. New data on the system Na_2CO_3–$CaCO_3$–$MgCO_3$ at 6 GPa with implications to the composition and stability of carbonatite melts at the base of continental lithosphere. *Chem. Geol.* **2019**, *515*, 50–60. [CrossRef]
52. Logvinova, A.M.; Shatskiy, A.; Wirth, R.; Tomilenko, A.A.; Ugap'eva, S.S.; Sobolev, N.V. Carbonatite melt in type Ia gem diamond. *Lithos* **2019**, *342–343*, 463–467. [CrossRef]
53. Sharygin, I.S.; Golovin, A.V.; Pokhilenko, N.P. Melt pockets in sheared garnet lherzolite xenoliths from the Udachnaya-East kimberlite pipe (Yakutia, Russia). In Proceedings of the 9th International Kimberlite Conference, Frankfurt, Germany, 10–15 August 2008. Extended Abstract No. 9IKC-A-00213.
54. Kamenetsky, V.S.; Kamenetsky, M.B.; Weiss, Y.; Navon, O.; Nielsen, T.F.D.; Mernagh, T.P. How unique is the Udachnaya-East kimberlite? Comparison with kimberlites from the Slave Craton (Canada) and SW Greenland. *Lithos* **2009**, *112*, 334–346. [CrossRef]
55. Golovin, A.V.; Sharygin, I.S.; Korsakov, A.V. Origin of alkaline carbonates in kimberlites of the Siberian craton: Evidence from melt inclusions in mantle olivine of the Udachnaya-East pipe. *Chem. Geol.* **2017**, *455*, 357–375. [CrossRef]
56. Arefiev, A.V.; Shatskiy, A.; Podborodnikov, I.V.; Behtenova, A.; Litasov, K.D. The system K_2CO_3–$CaCO_3$–$MgCO_3$ at 3 GPa: Implications for carbonatite melt compositions in the subcontinental lithospheric mantle. *Minerals* **2019**, *9*, 296. [CrossRef]
57. Arefiev, A.V.; Shatskiy, A.; Podborodnikov, I.V.; Litasov, K.D. Melting and subsolidus phase relations in the system K_2CO_3-$MgCO_3$ at 3 GPa. *High Press. Res.* **2018**, *38*, 422–439. [CrossRef]
58. Rashchenko, S.V.; Shatskiy, A.F.; Ignatov, M.A.; Arefiev, A.V.; Litasov, K.D. High-pressure synthesis and crystal structure of non-centrosymmetric $K_2Ca_3(CO_3)_4$. *CrystEngComm* **2021**, *23*, 6675–6681. [CrossRef]
59. Golubkova, A.; Merlini, M.; Schmidt, M.W. Crystal structure, high-pressure, and high-temperature behavior of carbonates in the $K_2Mg(CO_3)_2$–$Na_2Mg(CO_3)_2$ join. *Am. Mineral.* **2015**, *100*, 2458–2467. [CrossRef]
60. Pabst, A. Synthesis, properties, and structure of $K_2Ca(CO_3)_2$, buetschliite. *Am. Mineral.* **1974**, *59*, 353–358.
61. Hasterok, D.; Chapman, D.S. Heat production and geotherms for the continental lithosphere. *Earth Planet. Sci. Lett.* **2011**, *307*, 59–70. [CrossRef]
62. Katsura, T. A revised adiabatic temperature profile for the mantle. *J. Geophys. Res. Solid Earth* **2022**, *127*, e2021JB023562.
63. Eggler, D.H. Peridotite-Carbonate Relations in the System CaO-MgO-SiO_2-CO_2. *Carnegie Inst. Wash. Yearb.* **1975**, *74*, 468–474.
64. Wyllie, P.J.; Huang, W.L. Inflence of mantle CO_2 ingeneration of carbonatites and kimberlites. *Nature* **1975**, *257*, 297–299. [CrossRef]

65. Brey, G.; Brice, W.R.; Ellis, D.J.; Green, D.H.; Harris, K.L.; Ryabchikov, I.D. Pyroxene-carbonate reactions in the upper mantle. *Earth Planet. Sci. Lett.* **1983**, *62*, 63–74. [CrossRef]
66. Dalton, J.A.; Presnall, D.C. Carbonatitic melts along the solidus of model lherzolite in the system CaO-MgO-Al_2O_3-SiO_2-CO_2 from 3 to 7 GPa. *Contrib. Mineral. Petrol.* **1998**, *131*, 123–135. [CrossRef]
67. Shatskiy, A.; Podborodnikov, I.V.; Arefiev, A.V.; Bekhtenova, A.; Vinogradova, Y.G.; Stepanov, K.M.; Litasov, K.D. Pyroxene-carbonate reactions in the $CaMgSi_2O_6 \pm NaAlSi_2O_6 + MgCO_3 \pm Na_2CO_3 \pm K_2CO_3$ system at 3-6 GPa: Implications for partial melting of carbonated peridotite. *Contrib. Mineral. Petrol.* **2021**, *176*, 34. [CrossRef]
68. Shatskiy, A.; Bekhtenova, A.; Arefiev, A.V.; Podborodnikov, I.V.; Vinogradova, Y.G.; Rezvukhin, D.I.; Litasov, K.D. Solidus and melting of carbonated phlogopite peridotite at 3-6.5 GPa: Implications for mantle metasomatism. *Gondwana Res.* **2022**, *101*, 156–174. [CrossRef]
69. Shatskiy, A.; Bekhtenova, A.; Podborodnikov, I.V.; Arefiev, A.V.; Vinogradova, Y.G.; Litasov, K.D. Solidus of carbonated phlogopite eclogite at 3-6 GPa: Implications for mantle metasomatism and ultra-high pressure metamorphism. *Gondwana Res.* **2022**, *103*, 188–204. [CrossRef]
70. Wyllie, P.J.; Huang, W. Peridotite, kimberlite, and carbonatite explained in the system CaO-MgO-SiO_2-CO_2. *Geology* **1975**, *3*, 621–624. [CrossRef]
71. Brey, G.P.; Bulatov, V.K.; Girnis, A.V. Melting of K-rich carbonated peridotite at 6-10 GPa and the stability of K-phases in the upper mantle. *Chem. Geol.* **2011**, *281*, 333–342. [CrossRef]
72. Bekhtenova, A.; Shatskiy, A.; Podborodnikov, I.V.; Arefiev, A.V.; Litasov, K.D. Phase relations in carbonate component of carbonatized eclogite and peridotite along subduction and continental geotherms. *Gondwana Res.* **2021**, *94*, 186–200.
73. Litasov, K.D.; Shatskiy, A.; Ohtani, E.; Yaxley, G.M. The solidus of alkaline carbonatite in the deep mantle. *Geology* **2013**, *41*, 79–82. [CrossRef]
74. Shatskiy, A.; Podborodnikov, I.V.; Arefiev, A.V.; Litasov, K.D.; Chanyshev, A.D.; Sharygin, I.S.; Karmanov, N.S.; Ohtani, E. Effect of alkalis on the reaction of clinopyroxene with Mg-carbonate at 6 GPa: Implications for partial melting of carbonated lherzolite. *Am. Mineral.* **2017**, *102*, 1934–1946. [CrossRef]
75. Enggist, A.; Luth, R.W. Phase relations of phlogopite and pyroxene with magnesite from 4 to 8 GPa: KCMAS–H_2O and KCMAS–H_2O–CO_2. *Contrib. Mineral. Petrol.* **2016**, *171*, 88. [CrossRef]